

Investigation of Dielectric Properties for Structurally Modified Barium Titanate Near Ferro-Paraelectric Phase Transition

M.Sc. Thesis

By

PRASHANT JOSHI



**DISCIPLINE OF PHYSICS
INDIAN INSTITUTE OF TECHNOLOGY
INDORE
MAY, 2025**

Investigation of Dielectric Properties for Structurally Modified Barium Titanate Near Ferro-Paraelectric Phase Transition

A Thesis

*Submitted in partial fulfillment of the requirements for
the award of the degree*

of

Master of Science

By

Prashant Joshi

(Roll No. 2303151024)

Under the guidance of

Prof. SOMADITYA SEN



**DISCIPLINE OF PHYSICS
INDIAN INSTITUTE OF TECHNOLOGY
INDORE
MAY, 2025**



INDIAN INSTITUTE OF TECHNOLOGY INDORE

CANDIDATE'S DECLARATION

I hereby certify that the work which is being presented in the thesis entitled **Investigation of structurally modified Barium Titanate near Phase Transition** in the partial fulfillment of the requirements for the award of the degree of **MASTER OF SCIENCE** and submitted in the **DISCIPLINE OF PHYSICS, Indian Institute of Technology Indore**, is an authentic record of my own work carried out during the time period from July 2023 to May 2025 under the supervision of **Prof. Somaditya Sen**, Professor, Department of Physics, IIT Indore. The matter presented in this thesis has not been submitted by me for the award of any other degree of this or any other institute.


20-05-2025

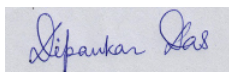
Signature of the student with date
Prashant

This is to certify that the above statement made by the candidate is correct to the best of my knowledge.



Signature of the Supervisor of
M.Sc. thesis
Prof. Somaditya Sen

PRASHANT has successfully given his M.Sc. Oral Examination held on **14 May, 2025**.



Convener, DPGC
Date: 20-05-25



Signature of the Supervisor of
M.Sc. thesis
Prof. Somaditya Sen

ACKNOWLEDGEMENT

First and foremost, I would like to express my sincere gratitude to the Department of Physics, Indian Institute of Technology Indore, for providing me with the opportunity and resources to carry out this research. I am also thankful to the Sophisticated Instrumentation Centre (SIC), IIT Indore, for facilitating Raman and DRS spectroscopy, which played a crucial role in my work. I am deeply indebted to my supervisor, Prof. Somaditya Sen, for his invaluable guidance, constant support, and encouragement throughout the course of my master's project. His expertise and mentorship have been instrumental in shaping this work. I would also like to extend my heartfelt thanks to my PhD seniors, especially my elder brother Dilip, and my sisters Maneesha, Manju, Rakhi, Poonam, and Tabinda, for their continuous motivation, technical help, and moral support at every step of this journey. A special note of gratitude to Prithviraj Bhaiya for his constant guidance, patience, and mentorship, which helped me navigate the challenges of this research. Lastly, I would like to thank my fellow interns and friends, Anmol, Anushka, and Aditya, for always being there to support and encourage me through every phase of this project. Also my Labmate Kartik for keeping my mental health on track.

This journey wouldn't have been the same without all of you. Thank you!

**DEDICATED TO MY COUNTRY,
INDIA**

ABSTRACT

Barium Titanate has been extensively studied for a long time as a model ferroelectric material. The Ferro-Paraelectric phase transition of this material is one of the complex problems in Solid-state Physics. This has attracted significant research attention over the past few decades, primarily because of their intriguing and poorly understood physical properties. Bearing in mind such an interest of investigation, Nickel has been doped into the A-site of Barium Titanate in this work. With the incorporation of this doping element, the dielectric properties of this material have been modified noticeably. The various compositions with this dopant have provided a wider platform to understand the versatility of the nature of transitions. The initial structural analysis has been performed using XRD, Raman, and FTIR spectroscopy to confirm the phase. Furthermore, DRS spectroscopy reveals the modification at the optical band structure. The morphological study has been done using scanning electron microscopy. With these understandings, the temperature and frequency-dependent Dielectric response has been recorded to understand the peculiarities of ferro-paraelectric phase transition. While the undoped sample shows a sharp feature, doping introduces disorder in the lattice, leading to a more diffuse transition. The evaluation of the AC conductivity reflects the evolution of different electrical transport mechanisms near the same. The overall study gives a brief insight into the intricacies of dielectric properties for structurally modified Barium Titanate near ferro-paraelectric phase transition.

List of Publications:

1. Estimating Diffuseness for the Non-Relaxor Type Ferroelectric to Paraelectric Phase Transition in BaTiO₃, Prithwiraj Ganguly, Prashant Joshi, Maneesha Puthiyoth, Somaditya Sen* [Arxiv][<https://arxiv.org/abs/2505.08270>].

Table of Contents

List of figures

List of Tables

Chapter 1:

Introduction.....

1.1: Introduction

1.2: Project Motivation

1.3: Material Reviews

1.3.1: Perovskites

1.3.2: Barium Titanate

- **Crystal structure of Barium Titanate**
- **Phase transition in Barium Titanate**
- **Hexagonal Phase in Barium Titanate**

1.3.3: Nickel as a Substitute

Chapter 2: Phase transitions in Ferroelectrics.....

2.1: Landau Theory

2.2: Classifications of Phase Transitions

2.2.1: 1st and 2nd order transitions

2.2.2: Order-Disorder and Displacive Transitions

2.2.3: Proper and Improper Ferroelectrics

2.3: Type of transition

2.3.1: Normal phase transition

2.3.2: Relaxor phase transition

2.3.3: Diffused phase transition

Chapter3: Characterization techniques.....

3.1: Introduction

3.2: X-ray Diffraction

3.2.1: Reitvalt Refinement

3.3: Raman Spectroscopy

3.4: Fourier Transform Infrared Spectroscopy (FTIR)

3.5: Field emission scanning electron microscopy (FE-SEM)

3.6: Diffuse Reflectance spectroscopy (DRS)

3.7: Dielectric Spectroscopy

- 3.7.1: Factors affecting dielectric constant
- 3.7.2: Conducting loss in dielectric material
- 3.7.3: AC conductivity of dielectric material
- 3.7.4: Nquist plots and Relaxation time

Chapter4:

Experimental.....

- 4.1: Synthesis: Sol-Gel method
- 4.2: XRD Analysis
 - 4.2.1: Lattice parameters
 - 4.2.2: Strain and Crystallite Size
- 4.3: Raman spectroscopy analysis
 - 4.3.1: Temperature-dependent Raman spectroscopy analysis
- 4.4: FTIR analysis
- 4.5: Band gap and Urbach energy analysis
- 4.6: Morphology of samples
- 4.7: Dielectric constant
 - 4.7.1: Room temperature analysis
 - 4.7.2: Temperature-dependent analysis near phase transition
 - Dielectric constant and tan delta
 - Relaxation time and disorder
 - AC conductivity and transport mechanism

Chapter 5: Future aspects and Conclusion.....

Chapter 6:Extra Work.....

BIBLIOGRAPHY

List of figures

Fig 1.1: Structure of perovskite

Fig 1.2: Applications of Perovskites

Fig 1.3: Crystal structure of Barium Titanate

Fig 1.4: Ionic radii of Barium, Titanium and oxygen ions

Fig 1.5: Different phases of Barium Titanate

Fig 1.6: Schematic of the distribution of Ti-displacement

Fig 1.7: d^2sp^3 hybridisation of Ti^{4+} ion

Fig 1.8: Formation of bond in Barium Titanate

Fig 1.9: Hexagonal phase of Barium Titanate

Fig 1.10: Formation of Ti_2O_9 dimer

Fig2.1: Evolution of $F(P)$ with temperature in (a) First order phase transition and (b) Second order phase transition using Landau theory

Fig2.2: Schematic of temperature-dependent evolution of $\epsilon'_r(T)$, $1/\epsilon'_r(T)$, and P_s for (a) First-order transition and (b) Second-order transition

Fig 2.3: Schematic representation of Order disorder and Displacive type transitions

Fig 3.1: Bruker D2 Phaser x-ray diffractometer

Fig 3.2: Diffraction from Bragg's planes

Fig 3.3: Horiba LabRAM HR Raman Spectrometer

Fig: 3.4 Stokes and Anti-Stokes scattering in Raman Spectroscopy

Fig 3.5: FTIR (Bruker: Tensor 27)

Fig 3.6: Supra 55 FESEM

Fig 3.7: Schematic working of FESEM and penetration of electrons in the sample

Fig 3.8: PSM 1735 Impedance analyzer

Fig 3.9: Conducting losses in Dielectrics

Fig 4.1: Schematic diagram to show the Sol-Gel process

Fig 4.2: Fractional ratio of P_{63}/mmc Hexagonal phase and non-stoichiometric phase

Fig 4.3: X-ray diffraction pattern for a set of samples calcinated at 1200 °C

Fig 4.4: Reitvald Refinement of $Ba_{1-x}Ni_xTiO_3$ for $x=0, 0.03125, 0.0625, 0.125$ and 0.25

Fig 4.5: Lattice parameters, cell volume, and Tetragonality variations with composition

Fig 4.6: Fitting of Williamson-Hall plot from refined data

Fig 4.7: Variation of Crystallite size, dislocation density, and microstrain with doping

Fig 4.8: Raman spectra of Nickel modified Barium Titanate

Fig 4.9: Temperature-dependent Raman spectra of all samples

Fig 4.10: a. FTIR spectra of all samples b. Modifications in the wavenumber associated with the Ti-O bond

Fig 4.11: Absorbance spectra of all samples using DRS

Fig 4.12: a) Bandgap variation with doping, b) Urbach energy variation with doping

Fig 4.13: Morphology of all samples and particle size variation with doping

Fig 4.14: Variation of Dielectric constant and $\tan \delta$ at room temperature

Fig 4.15: Temperature dependence of the Dielectric constant

Fig 4.16: Curie Temperature variation with doping

Fig 4.17: Plot of the inverse of epsilon with temperature

Fig 4.18: Deviation between T_m and T_b

Fig 4.19: Fitting of Modified Curie-Weiss law

Fig 4.20: Variation of γ and δ with doping

Fig 4.21: Bode's plot from Temperature range (50 °C- 140 °C)

Fig 4.22: Variation of relaxation time with Temperature

Fig 4.23: Temperature-dependent AC conductivity plot for all samples

Fig 4.24: Fitting of Arrhenius relation in DC conductivity

Fig 4.25: Variation of exponential parameter with temperature

Fig 6.1: XRD of all the samples and evolution of 31° peak for each doping at different calcinating temperatures

Fig 6.2: Evolution of Raman spectra for each sample at different calcinating temperatures

Fig 6.3: Variation of non-stoichiometry with doping

Fig 6.4: XRD peaks for BaTi_2O_5 and BaTiO_3

Fig 6.5: Fitting of the Fano equation at 180 cm^{-1} interference dip in BaTiO_3

Fig 6.6: Plot of M-H Hysteresis loop for all samples

List of Tables

Table 1.1: Value of tolerance factor for different crystal structures

Table 4.1: Raman shift for different vibrational modes

Table 6.1: Fitting parameters of the Fano equation

CHAPTER 1: Introduction

Ferroelectric materials are a class of materials that exhibit spontaneous polarization, unlike ordinary dielectrics. This comes from the energetically favourable asymmetric atomic distortion in the unit cell or the electronic charge redistribution. Furthermore, the nearby dipoles then get aligned in the same direction within a domain. These domains introduce a non-linear dielectric response to the external electric field, which causes a net polarization (P_s) in the system, even if the field is switched off completely. This is the signature property for an FE material.

A prominent FE like BaTiO_3 (BTO) is one of such materials. In contrast, in 1970 Smolensky discovered that, with the introduction of Sn in BTO, the ϵ'_r peak becomes diffused over a wide temperature range, which gets broader with increasing Sn content. Also, the temperature corresponding to the dielectric maxima (T_m) shifts prominently towards higher temperatures with an increase in frequency, showing a pronounced dispersive nature before transition. Since then, numerous modified complex perovskite oxides e.g., $\text{Pb}(\text{Mg}_{1/3}\text{Nb}_{2/3})\text{O}_3$ (PMN) and $\text{Pb}(\text{Zn}_{1/3}\text{Nb}_{2/3})\text{O}_3$ (PZN) [1] have demonstrated very similar diffused phase transition (DPT). To investigate such a transition, Barium Titanate has been modified with Nickel and has been studied thoroughly.

1.2 Project Motivation

Barium Titanate (BaTiO_3) exists in the tetragonal $P4mm$ phase at room temperature, where the displacement of Ti^{4+} from its central position in the $(\text{TiO}_6)^{2-}$ octahedra gives rise to ferroelectricity. However, in the $\text{Pm}\bar{3}m$ cubic and $P6_3/mmc$ hexagonal phases, the structure is centrosymmetric, leading to the loss of ferroelectric behavior.

According to literature, doping with transition metals such as Nickel or Cobalt at the B-site often induces a structural transformation from the ferroelectric tetragonal phase to the non-ferroelectric hexagonal $P6_3/mmc$ phase[3]. This phase transition is likely driven by the difference in oxidation states between the dopant (e.g., Ni^{2+}) and the host Ti^{4+} ions.

There is limited literature available on A-site Nickel doping in Barium Titanate. The significant difference in ionic radii between Ba^{2+} and Ni^{2+} makes such substitution inherently unfavorable. Additionally, Nickel typically prefers a 6-fold coordination environment, which is incompatible with the 12-fold coordination of the A-site in the perovskite structure. Substituting an alkali-earth metal with a transition metal adds to the complexity. All these factors — ionic size mismatch, coordination incompatibility, and chemical dissimilarity — can introduce lattice strain and structural instability, potentially leading to the formation of a distribution of different phases.

Despite these limitations, A-site substitution offers a notable advantage—Nickel shares the same oxidation state (2^+) as barium. This charge compatibility helps preserve the tetragonal structure, preventing its transformation into centrosymmetric phases and thereby retaining the material's ferroelectric properties [5]. The substitution of Nickel introduces lattice strain or tension within the existing structure. Therefore, **the primary motivation for doping Nickel at the A-site is to deliberately induce structural disorder and composition fluctuations, without altering the crystallographic phase. This, in return, enables a focused investigation into the nature and extent of diffuseness associated with the phase transition.**

1.3 Material Reviews:

1.3.1 Perovskites

Perovskites have been attracting researchers for a few decades due to their stable crystal structure with numerous applications [Fig. 1.2]. Since the discovery in 1839 by Gustave Rose, these structures have shown a wide range of properties.

A → cation (having +1/+2/+3 oxidation state)

B → Transition metals (+5/+4/+3/+2 oxidation state)

O → Oxygen (-2 oxidation state)

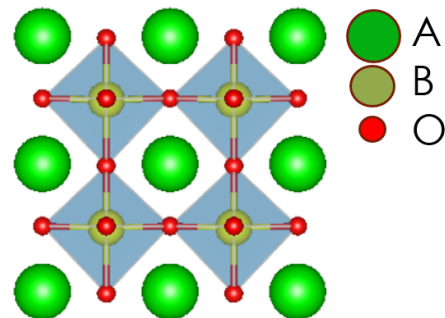


Fig 1.1: Structure of perovskite

Ideal perovskites(cubic structure) unit cells consist of a B atom at the center, A atom at the corner, and all the X's are face-centered, exhibiting 12, 6, and 2 coordination numbers, respectively. The B site atoms form an octahedral (BX₆) structure, whereas the A site is caged inside a tetragonal cavity.

- **Structures of perovskites**

Since Perovskites cover most of the periodic elements in it, they have variety in their crystal structures as well, they generally have Tetragonal, Cubic, Rhombohedral, Orthorhombic, and Hexagonal structures depending on the (i) atomic size of an atom, (ii) bond length between different atoms, (iii) distortions in the lattice and octahedra. To analyze the stability of the structure, the concept of the Tolerance factor [7] is introduced:

$$t = \frac{r_A + r_o}{\sqrt{2}(r_B + r_o)} \quad (1.1)$$

where ($r_a + r_o$) corresponds to the A-O bond length,

and ($r_b + r_o$) corresponds to the B-O bond length.

We can predict the crystal structure using this Tolerance factor within certain limitations by the table [1.1] [7] as follows:

Tolerance Factor	Structures	Examples
>1	Hexagonal Tetragonal	BaNiO ₃ BaTiO ₃
0.9-1	Cubic	SrTiO ₃
0.71-0.9	Rhombohedral Orthorhombic	GdFeO ₃ CaTiO ₃
<0.71	Mixture	FeTiO ₃

Table 1.1: Value of tolerance factor for different crystal structures

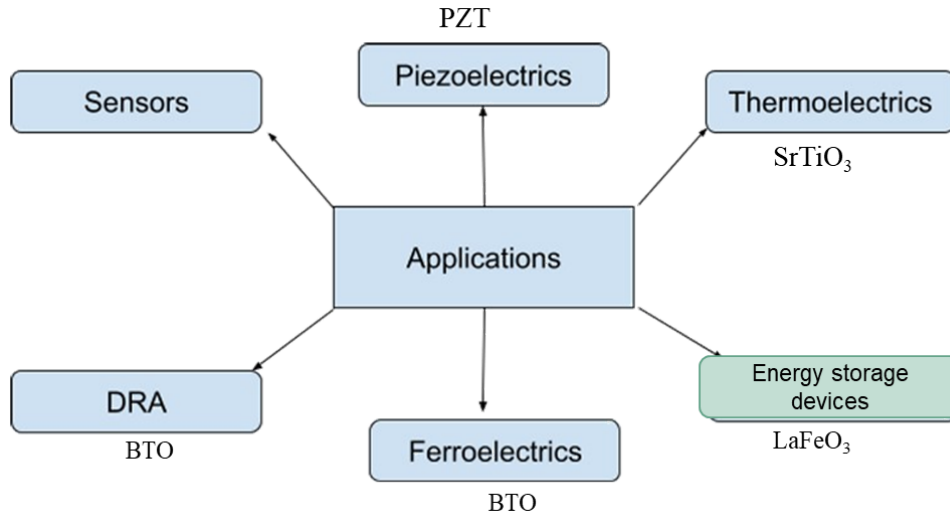


Fig 1.2: Applications of Perovskites

1.3.2 Barium Titanate

BaTiO₃ is popular among the perovskites due to its high dielectric constant. Ionic radii of Ba²⁺: 1.35 Å, Ti⁴⁺: 0.61 Å and O₂²⁻: 1.4 Å as per the literature. For BaTiO₃, the Ba²⁺ cations are located on the A-sites and Ti⁴⁺ on the B-sites with eight Ba²⁺ being on the corners at (0 0 0); (0 0 1); (0 1 0); (1 0 0); (1 0 1); (1 1 0); (0 1 1); (1 1 1). In cubic symmetry, the Ti⁴⁺ cations are positioned in the center at (½, ½, ½), while six O⁻ anions are at the center of the four faces at (0, ½, ½); (½, 0, ½); (½, ½, 0).

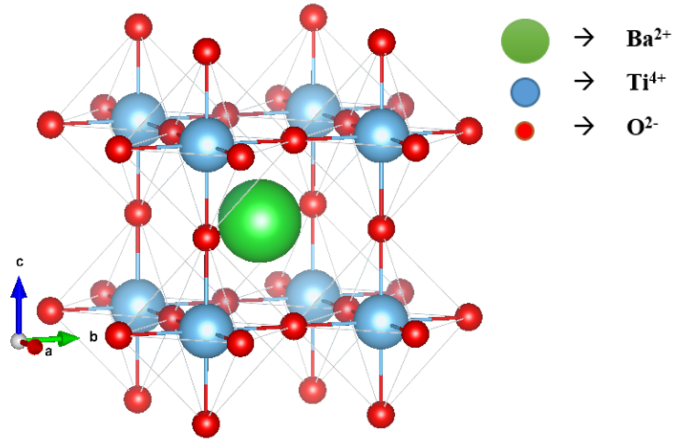


Fig 1.3: Crystal structure of Barium Titanate

Element	Ionic Radii	Coordination no
Ba^{2+}	1.35	12
Ti^{4+}	0.61	6
O_2^{2-}	1.4	2

Fig 1.4: Ionic radii of Barium, Titanium and Oxygen ions

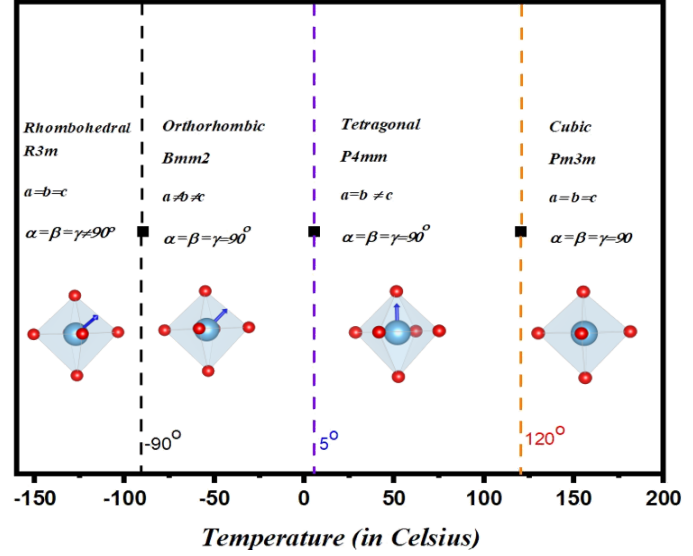


Fig 1.5: Different phases of Barium Titanate

● Crystal Structure of Barium Titanate

BTO undergoes a succession of phase transitions, from low to high temperature in the sequence, Rhombohedral (R3m)→ Orthorhombic (Amm2)→ Tetragonal (P4mm)→ Cubic (Pm-3m) perovskite phases with continuous increase of structural symmetry [8]. Among them, the FE to PE transition is associated with the asymmetric Tetragonal (T) to highly symmetric Cubic phase transformation. It is the distorted TiO_6 octahedra within a unit cell in the T-phase that generate a net resultant dipole moment along the c-axis. As reported by Grinberg et. Al [6], in all four phases, the distribution of the Ti-atom displacement from the octahedra centre is approximately a Gaussian curve instead of a sharp peak. The displacement along the c-axis (d_z) in the T-phase shifts toward lower values as the temperature increases, and finally, in the PE phase, it reaches a mean of zero. However, even though the distribution is centred at zero, it has the possibility of nonzero displacements too. It suggests that at high temperatures also some Ti atoms are still locally displaced. The experimentally observed net zero polarization is the result of an isotropic distribution of local dipoles along different directions.

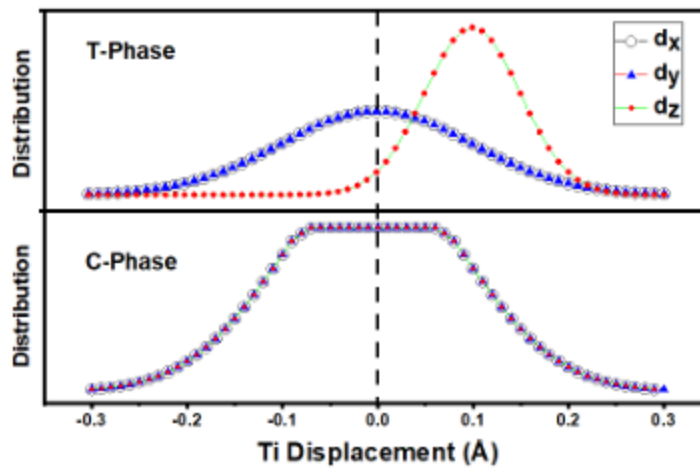


Fig 1.6: Schematic of the distribution of Ti-displacement

Since the net dipole moment in the cubic phase is zero, ferroelectricity vanishes in the cubic structure.

The Hexagonal structure of Barium Titanate can be obtained after calcinating the material over 1400 °C. Similar to the cubic phase, it also doesn't show any ferroelectricity.

● Explanation for the different phases of Barium Titanate using Bond Theory

In the TiO_6^{2-} octahedron, displacement of Ti^{4+} from the center position leads to different phases. In the cubic phase, the Titanium ion is located at the center of the octahedra. Because of that, the crystal field splits the five d-orbitals of the Titanium ion into two groups (as per crystal field theory): double degenerated e_g (d_z^2 , $d_{x^2-y^2}$) and triply degenerated t_{2g} (d_{xy} , d_{yz} , and d_{zx}) energy states. In this case, the e_g will have higher energy than t_{2g} because of ligand repulsion along the axes. Following the minimization of energy, the e_g orbitals hybridize with 1s and 3p orbitals, forming six equivalent atomic orbitals d^2sp^3 . These will form 6σ bonds with Oxygen-2p orbitals, hence shaping the skeleton of an Octahedra [9].

Hereafter, the available t_{2g} orbitals of Ti-atoms participate in π-bonding with 2p-π Oxygen orbitals in the direction

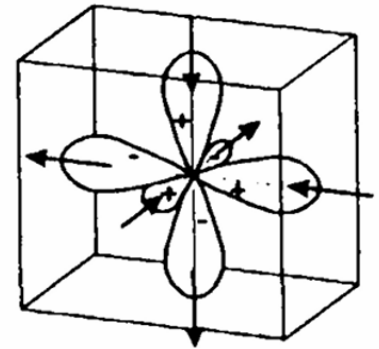


Fig 1.7: d^2sp^3 hybridisation of Ti^{4+} ion

perpendicular to the O-Ti-O bond. Hence, their formation in the structure is favourable and energetically advantageous when Titanium gets displaced from its centre position in non-cubic phases.

If there is a new covalent bond formed in the direction of [001] that leads to the shifting of Titanium along one of the edges, forming a tetragonal structure. Whereas, if two π bonds are involved (any two t_{2g} orbitals), the shifting will be towards one of the face diagonals [011] leading to orthogonal phase and in case of three orbitals (d_{xy}, d_{zx}, d_{yz}) it will become rhombohedral with the Titanium being shifted along the body diagonal [111] [10].

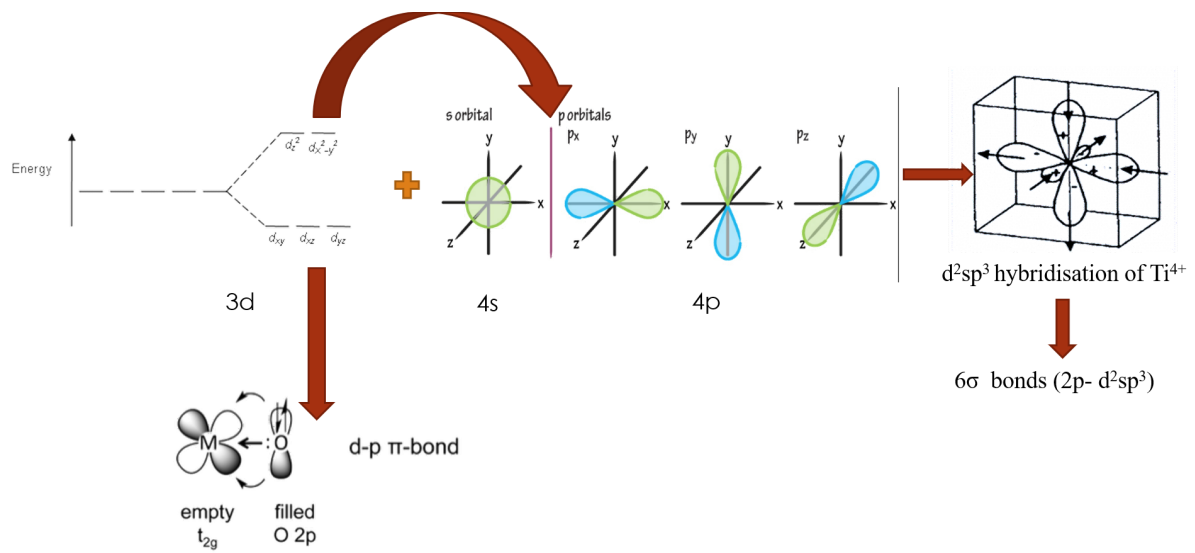


Fig 1.8: Formation of bond in barium Titanate

● Effect of Temperature on Phase Transition

The available literature concludes that from the first-order principal calculation, there are eight different lowest energy minima over the space diagonal. Along with that, some low barrier wells are on the side diagonal and smallest along the edge. So at the lower temperature, it resides under those 8 minima of body diagonal [16], hence giving the phase of rhombohedral, whereas increasing temperature enables them to go through face diagonal and ultimately reach the tetragonal structure [11]. On further heating, the sample will lead to a symmetric phase of cubic.

● Transition into Hexagonal Phase

On increasing the temperature to around 1400 °C, BTO transits into a hexagonal phase with the $P6_3/mmc$ space group. In this phase, the unit cell consists of eight corner shared Ti atoms and four edge shared Ti atoms of the first kind, Ti1 (blue color atoms), and four internal Ti atoms of the second type, Ti2 (pink color atoms). Both Ti1 and Ti2 atoms form two types of TiO_6 octahedra in terms of symmetry. Ti1 forms TiO_6 octahedra, which are symmetric in nature with six equal Ti-O bond lengths ~ 1.9905 Å. On the other hand, two neighboring octahedra of Ti2 atoms share a face of three O atoms, represented as O2 (red atoms). Such a conjunct pair of faces shared octahedra is generally called a dimer. These internal Ti2 atoms in the dimer form TiO_6 octahedra, which are distorted. The arrangement of these distorted TiO_6 octahedra is a result of the transformation from $P4mm$ to $P6_3/mmc$ structure. The distance between the Ti2 ions inside the dimer is close to ~ 2.8 Å for the hexagonal $BaTiO_3$ [13].

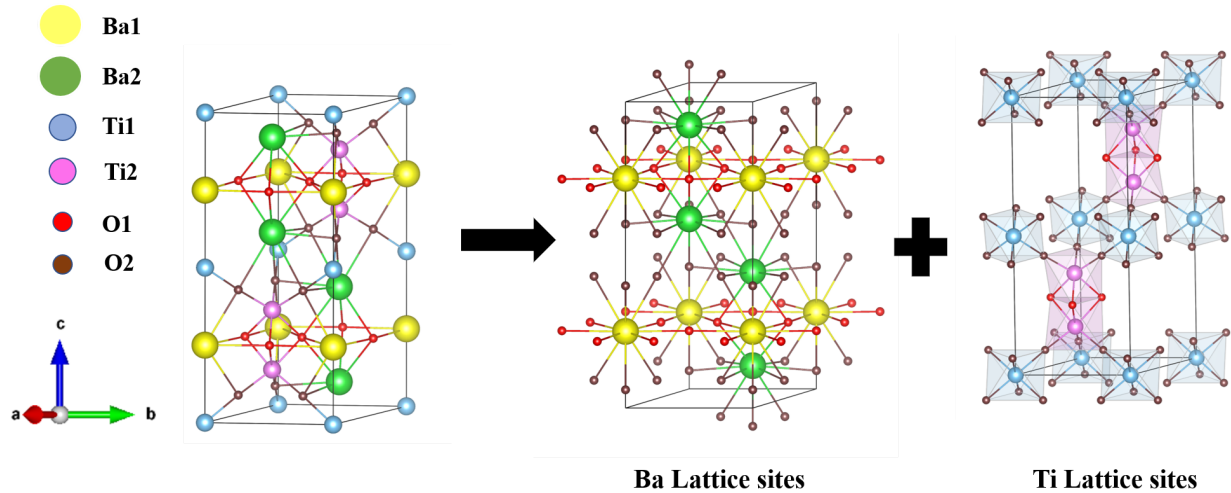


Fig 1.9: Hexagonal Phase of Barium Titanate

The repulsion between the two Ti2 atoms results in a longer Ti-O bond near the O3 face of the dimer, resulting in six Ti-O bonds ~ 1.992 Å and three shorter Ti-O bonds ~ 1.958 Å that are part of each Ti2 atom away from the O3 face. Hence, the two TiO_6 octahedra in the dimer are distorted, having three shorter and three longer Ti-O bonds. The relative displacement of the Ti2 ions with respect to the O-cage of the distorted TiO_6 octahedra in the hexagonal

BaTiO₃ is on opposite sides, thereby negating the possibility of ferroelectricity due to Ti ions [12].

Apart from the TiO₆ octahedra, the P6₃/mmc structure consists of a repeating pattern of three Ba-O planes [(Ba2-O1), (Ba1-O2), (Ba2-O1)]. In this, the consecutive Ba2 atoms are displaced from the O1 plane in the opposite direction along the c axis. Similarly, when considering the two consecutive Ba1-O2 planes of one repeating pattern with the Ba1O2 plane of the consecutive repeating pattern, there is minimal separation of Ba1 from the O2 plane in the opposite direction along the b axis. The displacement of Ba2 from the Ba2-O1 plane along the c direction is larger than that of the displacement of Ba1 from Ba1-O2 along the b direction. The displacement of two consecutive Ba1 atoms and two consecutive Ba2 atoms is displaced from the corresponding Ba-O plane in opposite directions and hence negates the possibility of ferroelectricity.

1.3.3 Nickel as a Substitute

Nickel is a lustrous metal with the chemical symbol Ni and atomic number 28. It has a relatively high atomic mass of 58.69 u and is known for its strength and durability. Physically, Nickel is dense, with a density of about 8.90 g/cm³, and has a high melting point of 1455 °C and a boiling point of 2913 °C. It is hard, malleable, and ductile, making it easy to shape into wires and sheets. One of its most notable characteristics is its resistance to corrosion and oxidation, especially in moist air, which makes it valuable in various industrial applications. Chemically, Nickel usually exhibits a +2 oxidation state but can also show +3 or 0 in some compounds. It reacts slowly with dilute acids and readily forms complex compounds. Nickel is also ferromagnetic, meaning it is magnetic at room temperature, with a Curie temperature of around 358°C, above which it loses its magnetism. In terms of electrical and thermal properties, it conducts both electricity and heat well. Mechanically, Nickel is tough and resistant to fatigue and impact, and it readily forms strong alloys with other metals like iron, chromium, and copper. These properties make Nickel an essential material in stainless steel, batteries, electronics, and aerospace applications.

As notified earlier, A site has a 12 coordination number. Nickel has ionic radii around 0.69 Å (for coordination number 6) as per Shannon's radii [14]. It has not been calculated for 12

12-coordination number. It is obvious too, as Nickel(II) (Ni^{2+}) has a relatively small ionic radius (~69 pm for high spin), so there simply isn't enough physical space around the metal center to accommodate 12 ligands without a lot of steric (crowding) strain.

Putting 12 ligands around a single small metal center leads to significant repulsion between the ligands, especially if they are bulky or charged. This makes such structures energetically unfavorable in a discrete complex.

Substituting Nickel into the A-site of the perovskite structure is expected to introduce significant lattice disorder due to the ionic size and coordination environment differences. However, since Nickel can exist in a +2 oxidation state, which is the same as that of Barium, its incorporation into the A-site does not lead to any net charge imbalance within the crystal lattice. Consequently, this substitution does not promote the formation of oxygen vacancies. Importantly, despite the substitution, the perovskite retains its original tetragonal phase; however, the incorporation of Nickel introduces lattice strain or tension within the existing structure. Therefore, the primary motivation for doping Nickel at the A-site is to deliberately induce structural disorder without altering the crystallographic phase, enabling a focused investigation into the nature and extent of diffuseness and other changes associated with the phase transition.

When Nickel is doped into the B-site of BTO, it replaces the Ti^{4+} ions. However, since Ni^{2+} possesses a lower valence state than Ti^{4+} , this substitution introduces a significant charge imbalance in the lattice. In order to maintain overall charge neutrality, the crystal compensates by creating oxygen vacancies.

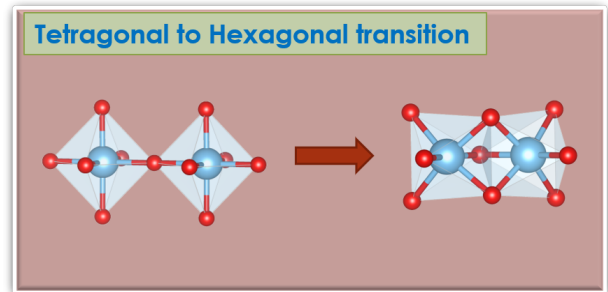
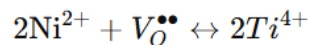


Fig 1.10: Formation of Ti_2O_9 dimer



These oxygen vacancies play a critical role in disrupting the long-range corner-sharing connectivity of the TiO_6 octahedra, which is a fundamental feature for stabilizing the perovskite structure. The loss of oxygen atoms compromises the integrity of the three-dimensional octahedral network, increasing structural instability.

To accommodate this local distortion while preserving the perovskite structure, the lattice undergoes a form of self-reconstruction. Specifically, two neighboring titanium-centered octahedra, each deficient in oxygen due to the vacancy formation, can merge through shared oxygen atoms. This results in the formation of a dimeric structure known as Ti_2O_9 (as shown in the Fig 1.9), in which the two TiO_6 octahedra share a face rather than just a corner. This localized structural adaptation helps to mitigate the destabilizing effects of oxygen vacancies and allows the material to partially retain its perovskite character despite the significant dopant-induced distortions.

CHAPTER-2:Phase-Transition in Ferroelectrics

A general phase transition is characterised by an anomalous discontinuity in a macroscopic parameter with a small change in the control parameters. The ferroelectric to Paraelectric phase transition is one of them. Ferroelectricity is a property exhibited by certain materials that possess a spontaneous electric polarization. On applying a sufficient amount of thermal energy, this phase gets transformed into the paraelectric phase at a particular temperature (T_C). This characteristic is analogous to ferromagnetism, where a material displays a permanent magnetic moment that gets transformed into a paramagnetic phase as a part of temperature evolution [17].

2.1: Landau theory

All the signature features of the FE phase along with its transformation into the PE phase, can be theoretically modelled with the help of the Landau theory. A symmetry-based theoretical analysis to explain the equilibrium behaviour near a phase transition was first deduced by him in his 1937 classic papers [39]. This phenomenological approach serves as a conceptual bridge between the microscopic models and the observed macroscopic phenomena, assuming spatial averaging of all the local fluctuations. Landau characterized the transition in terms of an order parameter, a physical entity that is finite in the low-symmetry (ordered) phase and tends to zero continuously once the symmetry is maximized (disordered). This formalism was widely used to explain magnetic phase transitions. Devonshire introduced the Landau formalism for the first time to explain long-range interactions of the FE system by considering the spatially uniform P as the order parameter [16]. The free energy (F), in the vicinity of the transition, is then expanded as a power series of the order parameter P as $F(P)$, retaining only symmetry-compatible terms:

$$F(P, T) = \frac{1}{2}a(T)P^2 + \frac{1}{4}bP^4 + \frac{1}{6}cP^6 + \dots \quad (2.1)$$

where,

$a(T)$: Temperature dependance coefficients

b,c: temperature-independent constants

P: polarization (order parameter)

Usually we assume, $a(T) = a_0(T-T_0)$, where: $a_0 > 0$

To find the equilibrium polarization P, we minimize F with respect to P, i.e, derive F w.r.t P and equate it to zero. The equilibrium is achieved at the minima of F(P), at a finite polarization,

$P = \pm P_s$, where P_s denotes the spontaneous polarization in the FE phase.

$$\frac{dF}{dP} = aP + bP^3 + cP^5 = 0 \quad (2.2)$$

On increasing the temperature, the minima shift to $P=0$, representing the non-polar PE phase. The coefficients a_0 and c are positive and have been verified experimentally. In the presence of an external field E, the modified free energy becomes

$$F(P, T) = F_0 + \frac{1}{2}aP^2 + \frac{1}{4}bP^4 + \dots - EP \quad (2.3)$$

Susceptibility (χ) can be related to the free energy by the following expression:

$$\chi = \left(\frac{\partial^2 F}{\partial P^2} \right)^{-1} \rightarrow \frac{1}{\epsilon_r} \propto \left(\frac{\partial^2 F}{\partial P^2} \right) \quad (2.4)$$

For $(T > T_C)$ $P = 0$ (paraelectric phase)

Hence,

$$\frac{1}{\epsilon_r} \propto \left(\frac{\partial^2 F}{\partial P^2} \right) = a_0(T - T_C) \rightarrow \epsilon_r \propto \frac{1}{(T - T_C)} \quad (2.5)$$

This is the general Curie-Weiss law, which can also be derived using fundamental solid state physics and by using analogy from magnetism.

But if $(T < T_C)$ in that case P will not remain zero, i.e, $P = \pm P_0$

Now applying a small electric field E, hence the free energy becomes,

$$F(P, T) = F_0 + \frac{1}{2}a(T)P^2 + \frac{1}{4}bP^4 + \frac{1}{6}cP^6 - EP \quad (2.6)$$

For the equilibrium condition, the derivative of F(P) must be zero. Also, assume perturbed E as a very minimal field and hence can be neglected in the derivative part.

$$\frac{dF}{dP} = aP + bP^3 + cP^5 = 0 \quad (2.7)$$

$$\frac{\partial^2 F}{\partial P^2} = a + 3bP^2 + 5cP^4 \quad (2.8)$$

also for simplicity keeping c=0(higher order value)

$$a + bP_0^2 = 0 \Rightarrow P_0^2 = -\frac{a}{b} = \frac{a_0(T_c - T)}{b} \quad (2.9)$$

Putting this value of P₀ in the double derivative part

$$\epsilon_r \propto (a + 3bP_0^2)^{-1} = \left(a + 3b \cdot \frac{a_0(T_c - T)}{b}\right)^{-1} = (a + 3a_0(T_c - T))^{-1} \quad (2.10)$$

Also, a= a₀(T-T_C)

$$\epsilon_r \propto (a_0(T - T_c) + 3a_0(T_c - T))^{-1} = (-2a_0(T - T_c))^{-1} \quad (2.11)$$

Thus,

$$\epsilon_r \propto \frac{1}{(T_c - T)} \text{ for } T < T_c \quad (2.12)$$

2.2: Classifications of Phase Transitions

The constant ‘b’ can be positive or negative, depending on the evolution of the polarization being continuous or discontinuous at T < T₀. This classifies the FE-PE transitions into two categories, i.e., First order (b<0) and second order (b>0) [17].

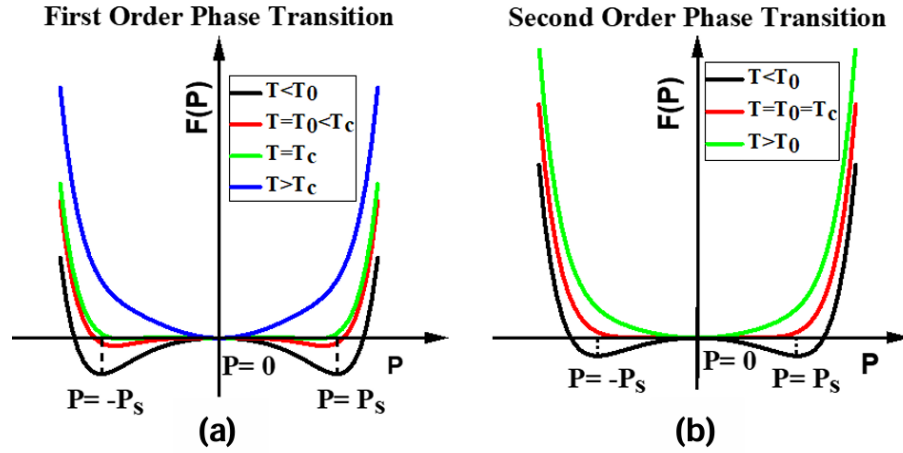


Fig2.1: Evolution of $F(P)$ with temperature in (a) First order phase transition and (b) Second order phase transition using Landau theory

A. 1st order phase transition

In the first-order phase transition, the P_s jumps discontinuously to zero in a sharp transition. Thus, the T_0 and T_c are not the same [Fig 2.1 (a)] [18]. Here, the spontaneous polarization and so the $F(P)$ minima at $P \neq 0$, do not get into the global minima of $P=0$ at T_0 . It decreases up to T_c , at which the shift to $P=0$ happens as a sudden occurrence, and explains the discontinuity in the P_s vs T plot. Note that, at T_0 , this global minimum is still not at $P=0$. Hence, here $T_0 < T_c$ [Fig 2.2 (a)].

B. 2nd-order phase transition

In the second-order phase transition, the two minima corresponding to the non-zero spontaneous polarization get continuously transformed to the $P=0$ phase at T_0 [Fig: 2.1 (b)]. Thus, the P_s continuously decreases up to this temperature. Simultaneously, the polar FE phase also get transformed to the non-polar PE phase at the same temperature. So, in this case, $T_c \sim T_0$ [Fig 2.2 (b)].

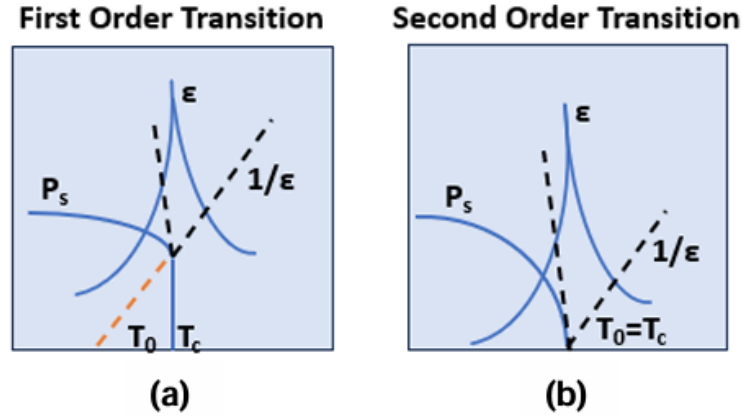


Fig2.2: Schematic of temperature dependent evolution of $\epsilon'_r(T)$, $1/\epsilon'_r(T)$, and P_s for (a) First order transition and (b) Second order transition

(ii) Order-disorder and displacive transition

The displacive phase transition in BaTiO_3 is primarily driven by the off-center displacement of the titanium (Ti) ion from its high-symmetry position within the oxygen octahedron of the perovskite lattice. At temperatures above the Curie point (approximately 393 K or 120°C), BaTiO_3 adopts a cubic perovskite structure. Upon cooling below this temperature, the Ti ion progressively shifts from the center, resulting in a series of structural phase transitions to tetragonal, orthorhombic, and rhombohedral phases at lower temperatures. This displacement of ions creates an asymmetry in charge distribution, resulting in the development of a spontaneous electric dipole moment and hence ferroelectricity. This type of transition, where the symmetry changes due to small atomic displacements, is a hallmark of displacive phase transitions.

In displacive-type phase transitions, the structural change is linked to the softening of a specific phonon mode, typically the $E(\text{TO}+\text{LO})$ mode, characterized by the relative movement of the titanium (Ti) ion within the oxygen octahedron, a displacement that plays a key role in the emergence of spontaneous polarization. As temperature increases toward the phase transition point, the frequency of this mode decreases and eventually vanishes beyond the transition. The presence and temperature-dependent behavior of this soft mode serve as a

hallmark of the displacive ferroelectric mechanism and can be effectively monitored through temperature-dependent Raman spectroscopy [19].

Order-disorder type transitions are characterized by the presence of permanent electric dipoles within each unit cell of the crystal lattice, even in the paraelectric phase. Diffuse X-ray scattering data suggest that the transition also occurs via an order-disorder transition (microscopically polar) mechanism. In this scenario, the overall crystal structure remains the same, but the dipoles become thermally randomized. Neutron diffraction and NMR were performed on the crystals, doped with paramagnetic centres. These studies have revealed the existence of strong anharmonicity of the local potential of Ti ions [15][20].

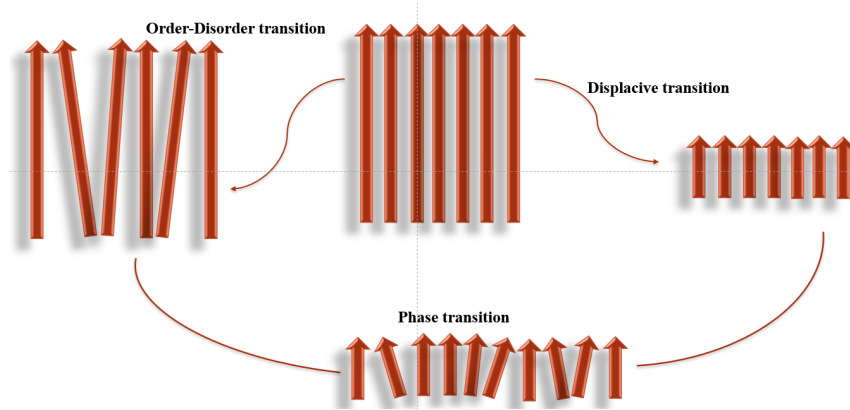


Fig 2.3: Schematic representation of Order disorder and Displacive type transitions

A key distinction between these two types of transitions lies in the state of the material above the Curie temperature. In order-disorder ferroelectrics, local dipoles persist in the paraelectric phase but are dynamically disordered. In displacive ferroelectrics, there are typically no permanent dipoles in the paraelectric phase; they emerge only with the structural distortion below T_c . However, it is important to note that the classification is not always absolute, and many ferroelectric materials exhibit characteristics of both order-disorder and displacive behavior. Along with that, theoretical studies also provide substantial proof for the coexistence of both mechanisms in the case of BTO.

(iii) Proper and Improper ferroelectrics

In proper ferroelectrics, the spontaneous electric polarization (P) acts as the primary order parameter that drives the phase transition from the higher-symmetry paraelectric phase to the lower-symmetry ferroelectric phase [21]. The transition occurs because the paraelectric phase becomes unstable with respect to the development of this intrinsic polarization, indicating a fundamental tendency of the material to adopt a polar state below a critical temperature.

Improper ferroelectrics are distinguished by the fact that their spontaneous electric polarization (P) is a secondary order parameter [22]. It is not the primary driving force of the transition but rather is induced by a primary order parameter (q) that represents some other physical quantity, such as a specific lattice distortion or a particular type of magnetic ordering.

Temperature dependence of dielectric constant:

The dielectric constant quantifies the extent to which a material can be polarized in response to an electric field. As the temperature approaches T_C , thermal agitation begins to disorder the ferroelectric alignment, breaking down long-range dipole order. This process creates local dipoles that are no longer strongly coupled, making them more responsive to an external field. This increased freedom boosts the dielectric constant as T_C is approached.

Above T_C , the material undergoes a phase transition from the tetragonal ferroelectric phase to the cubic paraelectric phase, whereby the spontaneous polarization disappears.

Now, in the paraelectric phase, the different dipoles are no longer cooperative. Due to the presence of thermal agitations, the orientational response of the dipoles gets disturbed, making the system less polarizable. This, in turn, reduces the dielectric constant of the material with the rise in temperature according to:

$$\epsilon_r = \frac{C}{T - T_0} \quad (2.13)$$

It is known as the Curie law with C and T_0 being the Curie constant and temperature, respectively. However, in the modified BTO structure, the presence of compositional fluctuations and disorder modifies the sharp transition into a diffuse nature. In that scenario, the temperature response of the dielectric material no longer follows the ordinary Curie-Weiss law, bringing the requirement of modification.

Modified Curie-Weiss Law

To study the diffuse Ferro-Para transition, Uchino[31] proposed a model

$$\frac{1}{\varepsilon} = \frac{1}{\varepsilon_m} + \frac{(T-T_m)^\gamma}{2\varepsilon_m \delta^2} \quad (2.14)$$

where $\varepsilon \rightarrow$ dielectric constant at temperature,

$\varepsilon_m \rightarrow$ maximum dielectric constant at temperature T_m

$\gamma \rightarrow$ describes the amount of deviation of thermal behaviour compared to C-W law

$\delta \rightarrow$ informs on the degree of the peak spreading or temperature extension for DPT

These transitions follow the Curie-Weiss law and have a single Curie Temperature. The above model reduces to curie weiss law when $\gamma \rightarrow 1$. These types of transitions has been followed by those that have minimal amount of disorder in it.

2.3.2: Relaxor Phase transitions:

These ferroelectrics typically do not exhibit a single, well-defined Curie temperature (T_C). Instead, the distribution of T_C values generally follows a Gaussian profile, and by considering only the first two terms in its expansion, the system can be approximated with a diffuseness parameter approaching $\gamma \rightarrow 2$ in the earlier-mentioned equation [27]. Additionally, these materials show a strong frequency-dependent dielectric constant maxima at T_m . This behavior can be attributed to the presence of nano-polar regions (NPRs), whose size varies with the system's temperature. NPRs vanish at a characteristic temperature called the Berns temperature (T_B)[26], while their size grows as the temperature decreases, eventually freezing at the freezing temperature (T_f). Thus, the size and dynamics of nano-polar domains evolve

continuously with temperature. These regions interact with an external electric field, but their response depends on the oscillation speed of the field, meaning the measurement frequency. At low frequencies, PNRs have sufficient time to align with the field, causing the dielectric peak to appear at a lower temperature. Conversely, at higher frequencies, the PNRs cannot reorient quickly enough, leading to a shift of the dielectric peak toward higher temperatures. This frequency dependence can then be seen and estimated through the Vogel-Fulcher law [32].

$$f = f_0 \exp\left(-\frac{E_a}{K_B(T_m - T_f)}\right) \quad (2.15)$$

where, f = measurement frequency

T_m : temperature of maximum dielectric frequency

T_f : freezing temperature

E_a : activation energy

2.3.3: Diffuse Phased Transitions

These types of transitions are intermediate between normal ferroelectric and relaxor behavior. Instead of a sharp change at the phase transition, a broad peak is observed, similar to what is seen in relaxors. However, unlike true relaxors, no frequency dependence is detected in these samples, indicating the absence of nano-polar regions. The broad peak associated with a diffuse phase transition is often attributed to a distribution of Curie temperatures[29]. In such cases, the diffuseness parameter γ typically falls between 1 and 2 [28].

Reason of broadness: This phenomenon can be explained by the distribution of multiple Curie temperatures (T_C) within a single sample before reaching the T_{dev} (where the material fully transforms into the paraelectric phase). This behavior arises due to the presence of disorder in the sample. To break the dipole–dipole interactions within domains, a certain amount of activation energy is needed, which is provided by thermal energy. However, structural changes in the material can alter this required activation energy from domain to domain.

CHAPTER-3 Characterization Techniques

Ni-doped Barium Titanate has been synthesized using ($\text{Ni}_x\text{Ba}_{1-x}\text{TiO}_3$ for $x=0, 0.03125, 0.0625, 0.125$, and 0.25) and sintered at various temperatures ($T= 900^\circ\text{C}, 1000^\circ\text{C}, 1100^\circ\text{C}, 1200^\circ\text{C}$ and 1300°C respectively).

The obtained powder has been converted into densified pellets with a diameter of 10mm and a height of 1mm using a uniaxial hydraulic press (2 tons). Pellets were prepared with the addition of Polyvinyl Alcohol (PVA) to ensure proper adhesion of the particles. The set of pellets was sintered at different temperatures ($T= 900^\circ\text{C}, 1000^\circ\text{C}, 1100^\circ\text{C}, 1200^\circ\text{C}$ and 1300°C respectively) for 3 hours with a heating and cooling rate of $5^\circ\text{C}/\text{min}$. The pellets were pre-heated at 600°C for 6 hours to remove the PVA. These pellets are then further used for different characterizations described as follows:

A Bruker D2-Phaser X-Ray Diffractometer has been used to get the X-Ray Diffraction (XRD) data for structural analysis. A $\text{Cu K}\alpha$ source ($\lambda = 1.54 \text{ \AA}$) at 30 kV and 10 mA is used to take the data at the sweep rate of $0.50^\circ/\text{min}$ within the 20° to 80° range. The phonon modes were studied from room temperature and temperature-dependent Raman spectroscopy using a Horiba-made LabRAM HR Raman spectrometer (spectral resolution of 0.9 cm^{-1}). The illumination source was a He-Ne LASER of wavelength 632.8 nm. A CCD detector is used in backscattered mode along with a 600 grating. A Gemini Supra55 Zeiss Field Emission Scanning Electron Microscope (FESEM) was used to study the morphology. To avoid the charging effect, a metallic gold deposition ($\sim 5 \text{ nm}$) by sputtering techniques was required for charge drainage from the surface. The same pellets were used to estimate the dielectric properties using a broadband (100 Hz to 1 MHz) Newton's 4th Ltd. dielectric spectrometer. The spectrometer is equipped with a phase-sensitive multimeter having a signal strength of 1 V rms. All measurements are conducted at room temperature. Silver electrodes were painted using silver paste(room temperature cured) on both sides of the pellets for the dielectric measurements. A Shimadzu Diffused Reflectance Spectroscopy (DRS) having a wavelength range 200-1400nm is used to calculate the bandgap and Urbach tail for modified BTO. The Keithley 2450 Source meter has been used to analyze the IV characteristics for the samples.

3.2: X-ray diffraction

Model: Bruker D2 Phaser x-ray diffractometer **X-ray target:** Cu anode ($K_{\alpha}=1.5406 \text{ \AA}$)

Optics: Bragg Brentano, Parallel beam

MaxPower: 3 kW

Operating voltage: 30k

X-ray diffraction (XRD) is a powerful analytical technique used to determine a sample's composition or crystalline structure by analyzing the diffraction pattern of X-rays passing through the sample. XRD is extensively utilized in various fields, including materials science, chemistry, and geology, for characterizing organic and inorganic compounds, determining crystal structures, and identifying molecular arrangements

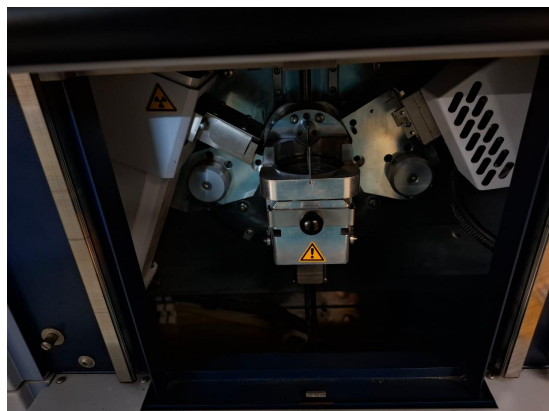


Fig 3.1: Bruker D2 Phaser x-ray diffractometer

Working

X-ray diffraction is a phenomenon where the uniformly spaced atoms in a crystal cause an interference pattern in an incoming beam of X-rays. Similar to how a diffraction grating affects light, the atomic planes in a crystal interact with X-rays. When an X-ray beam strikes a crystal at an angle θ , it reflects off the atomic planes at the same angle. These planes, spaced a distance d apart, must reflect the X-rays in such a way that the waves interfere constructively to produce a clear interference pattern. Constructive interference occurs when the difference in path length between rays reflected from successive planes equals an integer multiple (n) of the X-ray wavelength (λ), leading to the Bragg equation:

$$n\lambda = 2d \sin \theta \quad (3.1)$$

By analyzing the resulting diffraction pattern, scientists can determine the internal structure of the crystal.

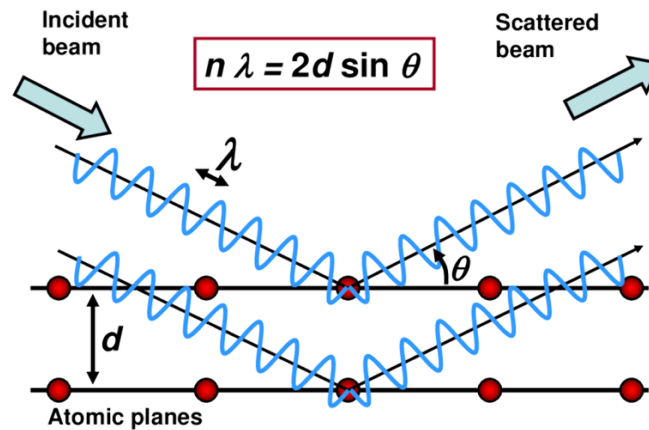


Fig 3.2: Diffraction from Bragg's planes

Lattice parameters:

XRD allows the determination of the size and shape of the unit cell, which is described by the lattice parameters (a , b , c , α , β , γ). These parameters are essential for identifying the crystal system and space group of the material. Cell Volume can also be calculated using these lattice parameters.

Lattice spacing: Interplanar spacing, often denoted as d , is the distance between two parallel atomic planes in a crystal lattice. These planes are imaginary but represent the regular, repeating arrangement of atoms in a crystal structure.

Crystallite Size: Crystallite size refers to the size of a single crystal domain within a polycrystalline material. In other words, it's the dimension of a region where the crystal lattice is continuous and unbroken by defects. Even though a material might look like a single solid crystal, it can actually be made up of many small crystallites, especially in powders, metals, or ceramics. Crystallite size is often determined using X-ray diffraction (XRD) data, particularly through the broadening of diffraction peaks. Smaller crystallites cause broader peaks.

Microstrain: Microstrain refers to tiny, localized distortions or deformations in a crystal lattice — essentially, how much the atomic spacing deviates from ideal due to internal stress, defects, or dislocations. Just like small crystallite size, microstrain also causes peak

broadening in XRD patterns. However, the broadening due to microstrain is different from that caused by size, and you can separate the two using methods like Williamson-Hall analysis, which considers both effects. If there exist multiple phases in a sample, XRD can tell you the percentage of each phase that exists in the sample.

3.2.1: Reitveld Refinement

Rietveld refinement is a powerful technique used to analyze and refine crystal structures from X-ray or neutron diffraction data. Rietveld refinement fits the entire diffraction pattern (peak positions, shapes, and intensities) to a theoretical model. It refines structural parameters to minimize the difference between observed and calculated patterns [33].

The theoretical model or experimentally verified diffraction data has been stored in the form of a Crystallographic Information file (CIF) in the ICDD(International Centre for Diffraction Data). Using that database as a reference, we refined our data by performing a least-squares fit to match their known structural model. In doing so, their original parameters were systematically adjusted to best align with our experimental data. This refinement process ultimately provided us with a new set of parameters that accurately describe our material.

The theoretical model consists of the following parameters:

- Structure Factor (Atomic and Geometrical Scattering Factor)
- Debye-Waller Factor (Temperature and Vibrational factor)
- FWHM parameters (u, v, and w)
- Shape Parameters (eta0 and X)
- Absorption Factor
- Preferred Orientation Factor
- Background
- Lorentz- Polarization Factor

Combining them all will contribute to the Intensity of a peak:

$$I_i^{calc} = S_F \sum_{j=1}^{N_{phases}} \frac{f_j}{V_j^2} \sum_{k=1}^{N_{peaks}} L_k |F_{k,j}|^2 S_j (2\theta_i - 2\theta_{k,j}) P_{k,j} A_j + bkg_i \quad (3.2)$$

3.3: Vibrational Spectroscopy (Raman Spectroscopy)

Model: Horiba-made LabRAM HR Raman spectrometer

Spectral Resolution: 0.9 cm⁻¹

Illumination Source: He-Ne LASER of wavelength 632.8 nm
Detector: CCD detector is used in backscattered mode along with a 600 grating

Raman spectroscopy is a powerful and versatile analytical technique used to study the vibrational, rotational, and other low-frequency modes of molecules. It provides valuable information about the chemical composition, molecular structure, and physical properties of a wide range of materials. Unlike infrared (IR) spectroscopy, which relies on the absorption of light, it is based on the inelastic scattering of monochromatic light, usually from a laser, by molecules in a sample. The technique was discovered in 1928 by the Indian physicist C.V. Raman, who was awarded the Nobel Prize in Physics in 1930 for this work. Raman observed that when a substance is illuminated with a monochromatic light source, a small fraction of the scattered light experiences a shift in wavelength. This shift, known as the Raman effect, is unique to the chemical bonds present in the material and provides a "chemical fingerprint" that can be used for identification and characterization.



Fig 3.3: Horiba LabRAM HR Raman Spectrometer

Instrumentation

A typical Raman spectrometer consists of the following components:

- **Excitation Source:** A laser, which provides a monochromatic light source. Common lasers include visible (e.g., 532 nm, 633 nm), near-infrared (e.g., 785 nm, 1064 nm), and ultraviolet lasers.
- **Sample Illumination System:** Lenses and mirrors that focus the laser beam onto the sample.
- **Sample Holder:** A platform or container to hold the sample.
- **Spectrometer:** A system to separate the scattered light by wavelength. This usually involves a grating that disperses the light.
- **Detector:** A sensitive detector, such as a charge-coupled device (CCD) or a photomultiplier tube (PMT), to measure the intensity of the scattered light at different wavelengths.
- **Computer and Software:** For data acquisition, processing, and analysis.

Working

When a monochromatic laser beam, typically in the visible or near-infrared range, is directed onto a sample, most of the light is scattered without any change in energy—this is known as Rayleigh scattering. However, a very small fraction of the light undergoes inelastic scattering, meaning it gains or loses energy by interacting with the vibrational energy levels of the molecules in the sample. This phenomenon is called Raman scattering. The energy shifts that occur correspond to the vibrational modes of the molecules and provide a unique spectral fingerprint that can be used to identify specific chemical bonds, molecular structures, and even crystalline phases.

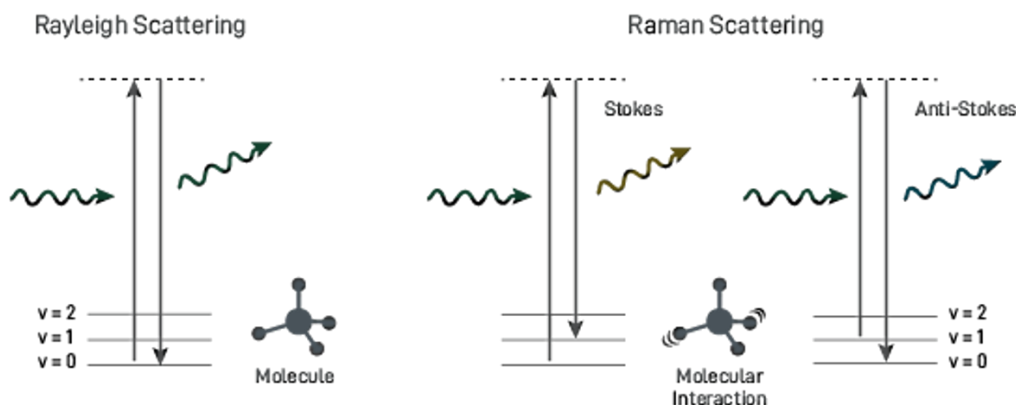


Fig: 3.4 Stokes and Anti-Stokes scattering in Raman Spectroscopy

Stokes Raman Scattering: Stokes scattering occurs when the scattered light has lower energy than the incident laser light, as the molecule absorbs part of the photon's energy and transitions from a lower to a higher vibrational energy level. In a Raman spectrum, Stokes lines appear on the lower-energy (longer wavelength) side of the laser line. These lines are typically more intense than anti-Stokes lines because, at room temperature, most molecules reside in their ground vibrational state, making upward transitions more probable.

Anti-Stokes Raman Scattering: Anti-Stokes scattering takes place when the scattered light has higher energy than the incident laser light, which occurs because the molecule starts in an excited vibrational state and loses energy by transferring it to the scattered photon as it relaxes to a lower energy level. In the Raman spectrum, anti-Stokes lines appear on the higher-energy (shorter wavelength) side of the laser line. These lines are generally weaker than Stokes lines, as relatively few molecules occupy excited vibrational states at room temperature.

3.4: Fourier Transform Infrared (FTIR) Spectroscopy

FTIR is an analytical technique used to identify and study chemical bonds and molecular structures through their interaction with infrared (IR) radiation. When a material is exposed to IR light, specific wavelengths are absorbed based on the vibrational modes of the molecules, corresponding to various functional groups.

FTIR operates on the principle that molecules absorb specific frequencies of infrared radiation, which correspond to the vibrational energies of their chemical bonds. When IR radiation passes through a sample, some of the radiation is absorbed at characteristic wavelengths, causing molecular vibrations such as stretching, bending, or twisting. Each functional group in a molecule



Fig 3.5: FTIR (Bruker: Tensor 27)

has a unique vibrational frequency, and thus an absorption pattern, which acts like a molecular "fingerprint." The absorbed IR light is recorded as a function of frequency (wavenumber) and converted into a spectrum. The Fourier Transform is applied to the raw interferogram (a time-domain signal collected from all wavelengths simultaneously), converting it into a readable frequency-domain spectrum.

Instrumentation

- a. IR Source: Emits broad-spectrum IR radiation (ex-, Silicon Carbide rod)
- b. Interferometer (Michelson Interferometer): Consists of a beam splitter, a fixed mirror, and a moving mirror, and modulates the IR light to produce an interferogram
- c. Sample Holder: Holds the sample (either KBr pellets or ATR(Attenuated Total Reflectance))
- d. Detector: It detects the IR radiation after it passes through the sample, such as Deuterated triglycine sulfate(DTGS)
- e. Computer and Fourier Transform Software: It processes the interferogram using a mathematical Fourier transform and outputs the final IR absorption spectrum.

3.5: Field emission Scanning electron microscopy (FESEM)

Model: Supra 55 Zeiss (Gemini Technology)

Operating Voltage: 0.02- 30 kV

Working upto: 100nA

Variable pressure mode: upto 133 Pa

The Field Emission Scanning Electron Microscope (FESEM) is an advanced imaging tool that plays a crucial role in high-resolution surface characterization, particularly in fields like nanotechnology, materials science, biology, and electronics. Its importance lies in its ability to produce detailed, three-dimensional-like images at the nanometer scale, allowing

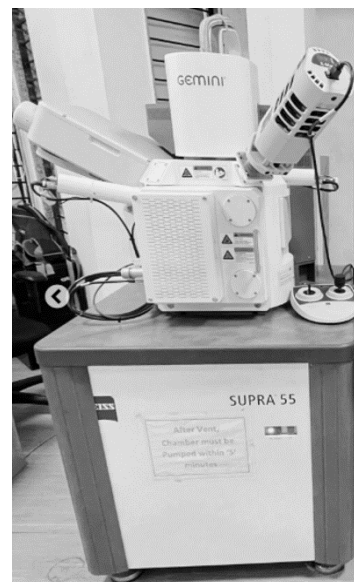


Fig 3.6: Supra 55 FESEM

researchers to observe surface structures with exceptional clarity.

FESEM operates on the basic principle of scanning electron microscopy, where a focused beam of electrons interacts with a specimen to generate signals that are used to form an image. Unlike conventional SEMs that use thermionic electron sources, FESEM employs a field emission gun (FEG), which emits electrons through a strong electric field rather than heat. This produces a much finer and more stable electron beam, significantly improving image resolution and contrast.

The main components of a FESEM include the field emission electron gun, a series of electromagnetic lenses to focus the beam, scanning coils that direct the beam across the sample, a vacuum specimen chamber, and various detectors to collect emitted signals. The entire system is controlled by advanced electronics and software that display the final image.

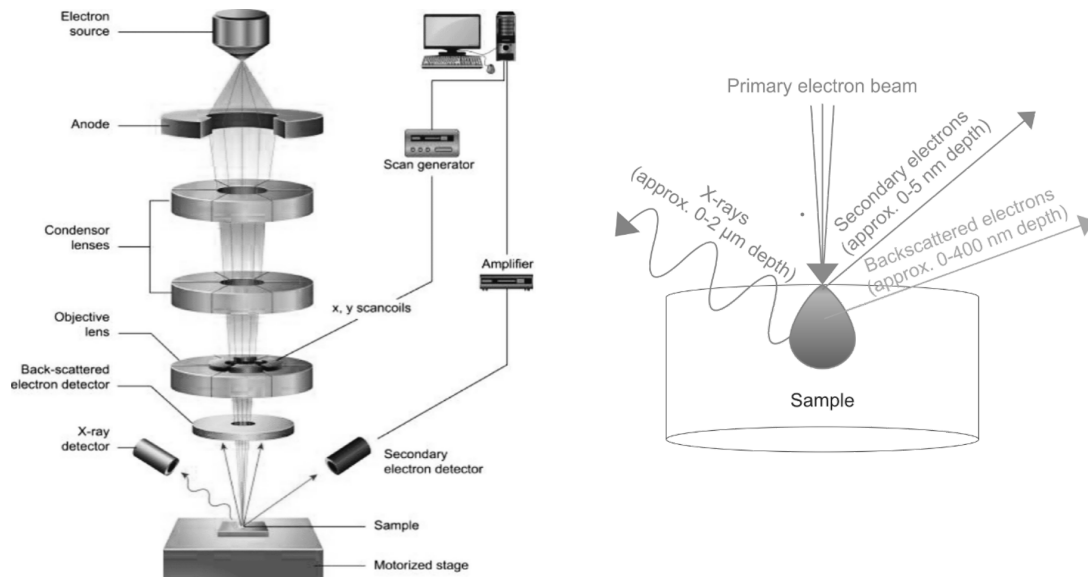


Fig 3.7: Schematic working of FESEM and penetration of electrons in the sample

In operation, the field emission gun emits a high-brightness electron beam that is finely focused by electron lenses. This beam is scanned across the sample surface in a raster pattern by the scanning coils. As the electrons strike the surface, they interact with the atoms in the sample, producing secondary electrons that are detected and used to create a detailed image.

The result is a high-resolution, high-contrast visualization of the surface morphology, which is invaluable for both research and industrial applications.

3.6: Diffuse Reflectance Spectroscopy (DRS)

Diffuse reflectance spectroscopy is a versatile tool that allows us to accurately measure the flux per wavelength of light reflected in a scattered manner from a sample. This scattering arises from the interaction of light with the sample's surface and internal structure, particularly when the material is powdered, granular, or rough.

DRS is particularly useful for analyzing solid samples that are difficult to measure using traditional transmission or specular reflection spectroscopy. It finds applications in various fields, including chemistry, materials science, environmental science, and pharmaceuticals.

Instrumentation

A typical DRS system includes the following components:

- **Light Source:** A broadband light source, such as a xenon lamp (for UV-Vis DRS) or a tungsten-halogen lamp (for Vis-NIR DRS).
- **Monochromator:** A device that separates the light into its individual wavelengths.
- **Integrating Sphere:** A hollow sphere coated with a highly reflective material (e.g., barium sulfate) that collects the diffusely reflected light from all angles and directs it to the detector.
- **Detector:** A detector that measures the intensity of the light, such as a photomultiplier tube (PMT) or a silicon photodiode.
- **Sample Holder:** A holder designed to accommodate solid samples, often with a specialized cup or window.
- **Reference Standard:** A highly reflective material with known reflectance properties (e.g., a white reflectance standard) used for calibration.
- **Computer and Software:** For data acquisition, processing, and analysis.

The most common method to measure diffuse reflectance is to use an integrating sphere that is mated with a spectrophotometer, allowing the measurement of both transmitted and reflected scatter. An integrating sphere is simply a hollow ball that has been coated (or is fabricated from a material) with a very highly reflective and diffuse surface on the inner diameter. The Reflectance can further be analyzed using the KUBELKA-MUNK Theory [35].

It simplifies the complex scattering and absorption processes within the sample into two parameters:

- **Absorption Coefficient (K):** Represents the rate at which light is absorbed by the sample.
- **Scattering Coefficient (S):** Represents the rate at which light is scattered by the sample.

The Kubelka-Munk function, derived from this theory, relates the reflectance (R) to the absorption and scattering coefficients:

$$F(R) = \frac{(1-R)^2}{2R} = \frac{K}{S} \quad (3.2)$$

The F(R) function is considered equivalent to the absorbance. And to calculate the band gap from it, Tauc formulates and gives rise to the Tauc plot [34], which is given by

$$(\alpha h\nu)^n = A(h\nu - E_g) \quad (3.3)$$

where,

$n \rightarrow$ Transition type ($n=2$ for direct and $\frac{1}{2}$ for indirect bandgap)

$E_g \rightarrow$ Band gap energy

$h\nu \rightarrow$ Photon energy

3.7: Dielectric Spectroscopy

Model: PSM 1735 Impedance Analyzer

Make: N4L

Range: 10 - 1MHz

Fixture: IAI Kelvin

Dielectric materials are basically insulating materials; however, calling them insulators doesn't meet the context here. Rather than conducting charge, they store energy in electrical form, indicating their charge-storing capability.

In dielectric materials, charge is not entirely free to move. When exposed to an external electric field, the material undergoes polarization, aligning in the opposite direction

of the applied field. This polarization generates an opposing electric field within the material, effectively reducing the overall internal electric field.

The dielectric properties of ceramic materials are typically measured using the parallel-plate capacitor technique at frequencies below 10 MHz. In this study, a broadband dielectric spectrometer (Newton's 4th Ltd.) was used to perform dielectric measurements over a frequency range of 100 Hz to 1 MHz.

The fundamental working principle of this impedance analyzer is based on the Wheatstone bridge configuration, where the material under investigation is placed alongside three known capacitances to determine its dielectric response accurately.

Polarization Mechanism

a) Electronic Polarization: Electronic polarization refers to the displacement of the electron cloud of an atom or ion relative to its nucleus under the influence of an external electric field. The nucleus travels in one direction while the electron cloud distorts in the opposite direction due to the applied field, which gives rise to the dipole moment.

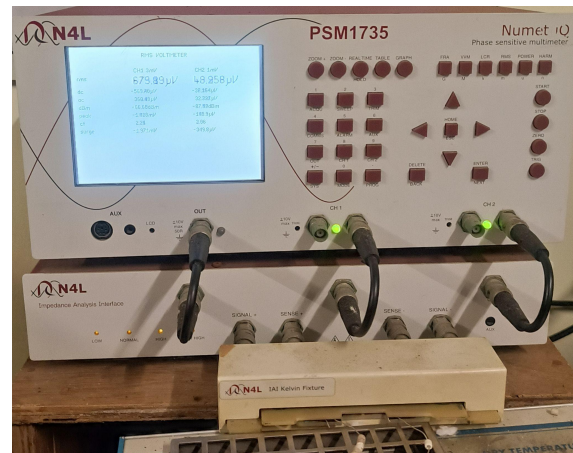


Fig 3.8: PSM 1735 Impedance analyzer

b) Ionic Polarization: Ionic polarization occurs in materials with ionic bonds, where an external electric field causes a relative displacement of cations (+) and anions (−), creating a net dipole moment.

c) Orientational Polarization: Certain molecules are always dipolar; that is, even when there is no electric field present, there is a charge separation inside the molecule, e.g., H_2O due to electronegativity differences.

d) Interfacial Polarization: Interfacial polarization, also called space charge polarization, occurs when mobile charge carriers (such as ions or electrons) accumulate at interfaces or defects within a material under an applied electric field.

3.7.1 Factors that affect the material's Dielectric Constant

(1) **Crystallite size:** A material with a large crystal size will have a high value of ϵ_r . This is because a bigger particle has more dipoles, which align when subjected to an electric field. This increases permittivity, which raises the value of ϵ_r [36][37].

(2) **Grain Boundaries:** A grain boundary is the interface where two different crystalline grains (or crystallites) meet within a polycrystalline material. These boundaries occur because individual grains in a material grow in different orientations during solidification or processing, and when they meet, their atomic structures do not perfectly align. Grain barriers trap charge carriers at interfaces, preventing them from moving; hence, a material with more grain boundaries will have a higher value of ϵ_r in the frequency range where interfacial polarization is active [38].

(3) **Porosity:** A thick substance that has sporadic air holes inside it is called a porous material. Porosity significantly affects the dielectric properties of a material, especially in ceramics, polymers, and composite dielectrics. Since pores are typically filled with air or vacuum (which has a very low dielectric constant, $\epsilon \approx 1$), they generally lead to a decrease in the effective dielectric constant (ϵ_{eff}) of the material [39].

(4) Crystalline defects:

(a) **Surface defects:** As the surface atoms are less bonded than the bulk, all surfaces are inherently defective(also called dangling bonds). The more these defects are, the more the polarization.

(b) **Vacancies:** Vacancies refer to missing atoms in the crystal. A material's high dielectric constant at low frequencies is a result of the vacancies' ability to trap charge carriers and create significant polarization, also known as space charge [40].

(c) **Substitution defect:** When a material is doped in the place of others, the ionic radii of the atom, electronegativity, etc, have a direct influence on the dielectric constant of the sample.

3.7.2: Conducting losses in a Dielectric medium

The dielectric constant is a complex quantity where the real part indicates its energy-storing contribution and the imaginary part represents the energy losses [41].

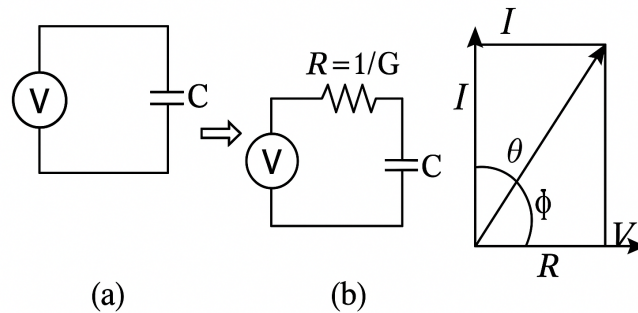


Fig 3.9: Conducting losses in Dielectrics

When supplied the voltage $V = V_0 \exp(j\omega t)$, the capacitance of the capacitor with the dielectric is given as $C = \epsilon_r C_0$, and the total current in the circuit (I) is a vector sum of charging current (I_C) and loss current (I_R). The charging current in the circuit is expressed as

$$I_c = j\omega \epsilon_r' C V \quad (3.4)$$

The loss current is expressed as:

$I_R = GV = V/R$, where G is the conductance. Let's define a complex dielectric constant s.t.

$$I_R = \omega \epsilon_r'' C_0 V, \quad (3.5)$$

Hence,

$$I = j\omega(\epsilon_r' - j\epsilon_r'')C_0V = j\omega\epsilon_rC_0V \quad (3.6)$$

The ‘dielectric loss’ or ‘dissipation factor’ for the dielectric material is expressed as the tangent of the loss angle δ i.e.

$$\tan\delta = I_R/I_C = \epsilon_r''/\epsilon_r' \quad (3.7)$$

3.7.3: AC Conductivity of Dielectric Material

AC conductivity is a measure of a material's ability to conduct an alternating current (AC).

σ_{AC} can be defined either in terms of impedance or calculated through the dielectric constants and tangent loss.

From the above expressions,

$$G = \omega\epsilon_r''C_0 \Rightarrow \sigma_{AC} = \omega\epsilon_0\epsilon''(\omega) \quad (3.8)$$

$$\sigma_{AC}(\omega) = \sigma_{DC} + A\omega^n \quad (3.9)$$

The above equation is known as the universal Jonscher power law[42], showing an increase in AC conductivity with an increase in frequency due to the hopping of charge carriers into nearest neighbouring sites or getting delocalized.

The pre-exponential factor “A” defines the strength of the polarizability.

The temperature dependence of the frequency exponent “n” can be correlated to the different possible transport mechanisms [50]:

- i. Correlated barrier hopping (CBH) in which “n” decreases continuously with temperature
- ii. Overlapping large polaron tunneling (OLPT) in which “n” decreases first and attains a minimum, and thereafter increases
- iii. Quantum mechanical tunneling (QMT) mechanism in which “n” is independent of temperature and generally has a value of 0.8
- iv. Non-overlapping small polaron tunneling (NSPT) model in which an increase in “n” is observed with the rise in temperature.

3.7.4: Nyquist plots (Cole-Cole Plot)

In general, the polycrystalline solids consist of grain and grain boundary regions. The grain (bulk) properties are quite different from the grain boundary characteristics. Thus, the charge transport mechanism, resistivity, and the macroscopic dielectric constant in polycrystalline materials represent the cumulative contribution of the sample-electrode interface, grain, and grain boundary characteristics. These contributions can be represented as equivalent parallel RC circuits connected in series. The resistance of each RC circuit represents the leakage current characteristics of the dielectric material, and C represents the charge storing characteristic.

The complex impedance data is represented as Nyquist plots, taking the real part (Z') of complex impedance in the X-axis and the imaginary part (Z'') of complex impedance in the Y-axis. In the Nyquist plot, the grain, grain boundary, and electrode interface contributions towards the electrical transport mechanism are depicted with different semicircles whose diameters give the time constant ($\tau=RC$) of each RC circuit associated with it. The semicircle at the high frequency side represents the grain contribution, and the semicircle at the low frequency side represents the grain boundary/electrode interface contribution towards the transport phenomena of the dielectric.

However, if only a single semicircle is present, the analysis can be effectively performed using Bode's plot method. In this approach, the imaginary part of impedance (Z'') is plotted against frequency, and the frequency at which Z'' reaches its maximum corresponds to the relaxation frequency associated with the characteristic relaxation time of the process. This can easily be derived using a single RC circuit and its analysis.

Relaxation time:

In the context of ferroelectrics, relaxation time refers to the time it takes for the electric polarization of the material to return to its equilibrium state once an external electric field is applied and then removed. It essentially estimates the delay in the polarization response on application of an external electric field. On application of an electric field, the electric dipoles within the ferroelectric material align themselves with the field. When you remove the field,

these dipoles don't instantaneously snap back to their original, random orientations. The relaxation time quantifies how long this reorientation process takes. This relaxation process is often frequency-dependent. At high frequencies, the dipoles may not have enough time to fully align and relax before the field reverses, leading to a phase lag between the applied field and the polarization.

CHAPTER-4 Experimental

4.1: Synthesis: Sol-Gel Route

Sol-gel process provides better control of the whole reaction involved during the synthesis of solids. Homogeneous multi-component systems can be easily obtained, particularly homogenous mixed oxides can be prepared by mixing the molecular precursor solutions. The sol-gel approach takes less time and a lower temperature to process and yields a satisfactory sample. Solid ion particles suspended in a colloidal solution (1nm- 1 μ m) in a solvent is called a sol. Sol evolves as an inorganic network containing a liquid phase, which is known as a gel. Metal oxides are formed by joining the metals with oxo or hydroxy chains. As a result, metal-oxo or metal-hydroxy polymer solutions are formed. The gel is then dried to remove the liquid phase from it, and finally forms a porous powder. After this, calcination and annealing may be carried out.

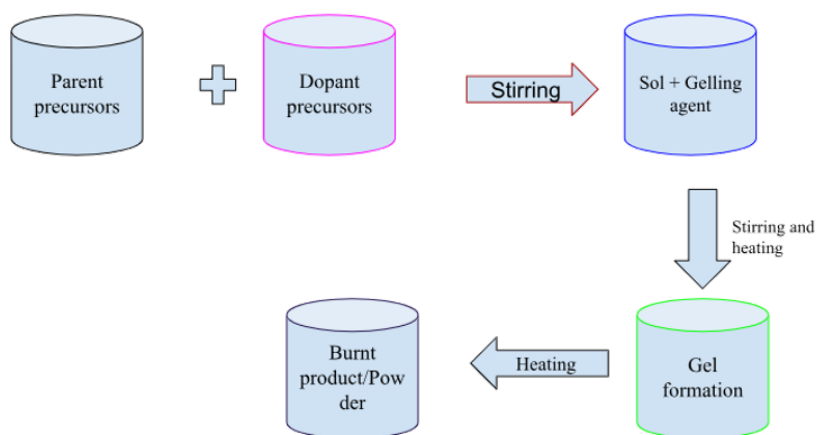


Fig 4.1: Schematic diagram to show Sol-Gel process

The following are the steps in the sol-gel process [44]:

Hydrolysis → Condensation → Gelation → Drying → Densification

A hydrolysis and polycondensation reaction takes place as follows.

Reaction involved

Hydrolysis: $\text{M-O-P} + \text{H}_2\text{O} \rightarrow \text{M-OH} + \text{P-OH}$

Water condensation: $\text{M-OH} + \text{HO-M} \rightarrow \text{M-O-M} + \text{H}_2\text{O}$

Alcohol Condensation: $\text{M-O-P} + \text{HO-M} \rightarrow \text{M-O-M} + \text{P-OH}$

The sol-gel-aided combustion method was used to prepare all the samples in this report. Samples were thermally treated as per the requirement of phase formation.

Since we are more interested in understanding how doping of Nickel affects the structure of BTO, a series of A-site Nickel doped Barium Titanate ($\text{Ni}_x\text{Ba}_{1-x}\text{TiO}_3$ for $x=0, 0.03125, 0.0625, 0.125$, and 0.25) has been synthesized using Sol-gel process where Barium nitrate, TALH, and Nickel Nitrate has been taken as precursors in the stoichiometric ratio. Citric acid and Ethylene glycol were used as a burning agent in a ratio of 1:2. For the removal of all the unwanted impurities, such as carbonates and nitrates, all the samples were put at 450°C and then 600°C for 6 hours. To get information on phase-forming temperature, a series of heat treatments were given (900° , 1000° , 1100° , 1200° , and 1300°C) for 3 hours.

4.2 XRD Analysis

It has been observed that for different heat treatments, the amount of hexagonality and non-stoichiometry differs. Hence the fractional percentage of Hexagonality and non-stoichiometry has been plotted.

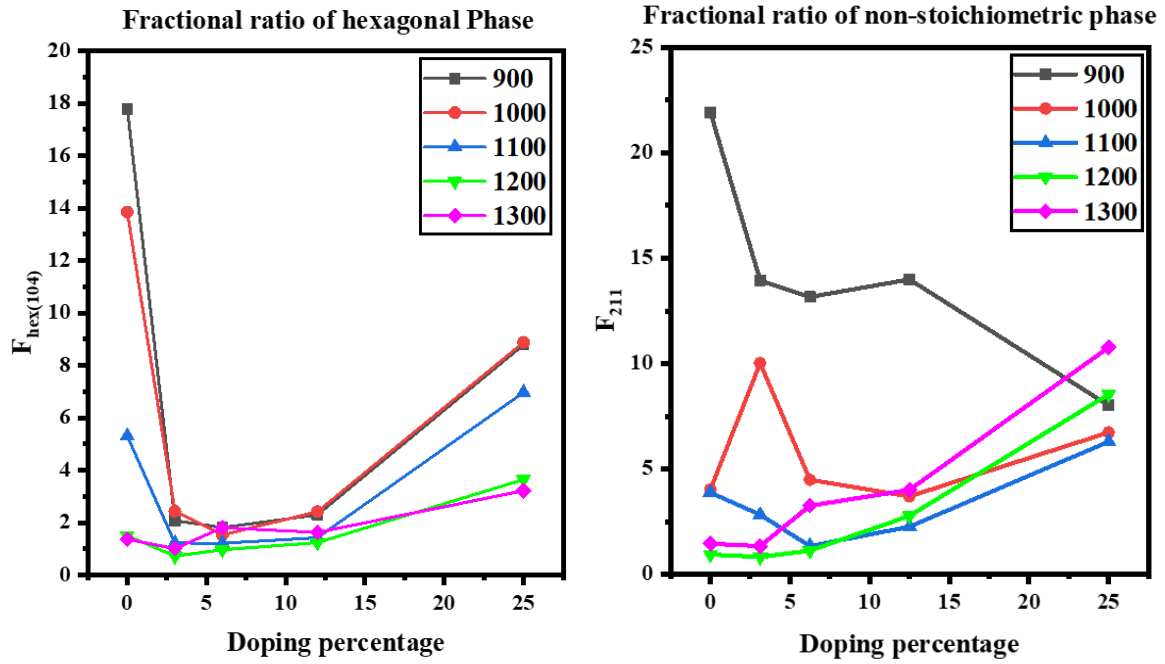


Fig 4.2: Fractional ratio of P_{63}/mmc Hexagonal phase and non-stoichiometric phase

$$F_{Hex} \% = \frac{I_{(104)Hex} * 100}{I_{(110)Tetra}}$$

$$F_{BaTi_2O_5} \% = \frac{I_{(104)BaTi_2O_5} * 100}{I_{(110)Tetra}}$$

The aim is to investigate for the maximum tetragonality in the sample. From the above plots, it can be easily concluded that the non-stoichiometric compound (suspected as $BaTi_2O_5$)[45] and the hexagonal $P_{63}mmc$ phase has been minimized in the sample which calcined at 1200°C. Hence this set of data $Ba_{1-x}Ni_xTiO_3$ for $x=0, 0.03125, 0.0625, 0.125, 0.25$ (termed as S1, S2, S3, S4 and S5 respectively) calcined as 1200°C has been taken for further investigations.

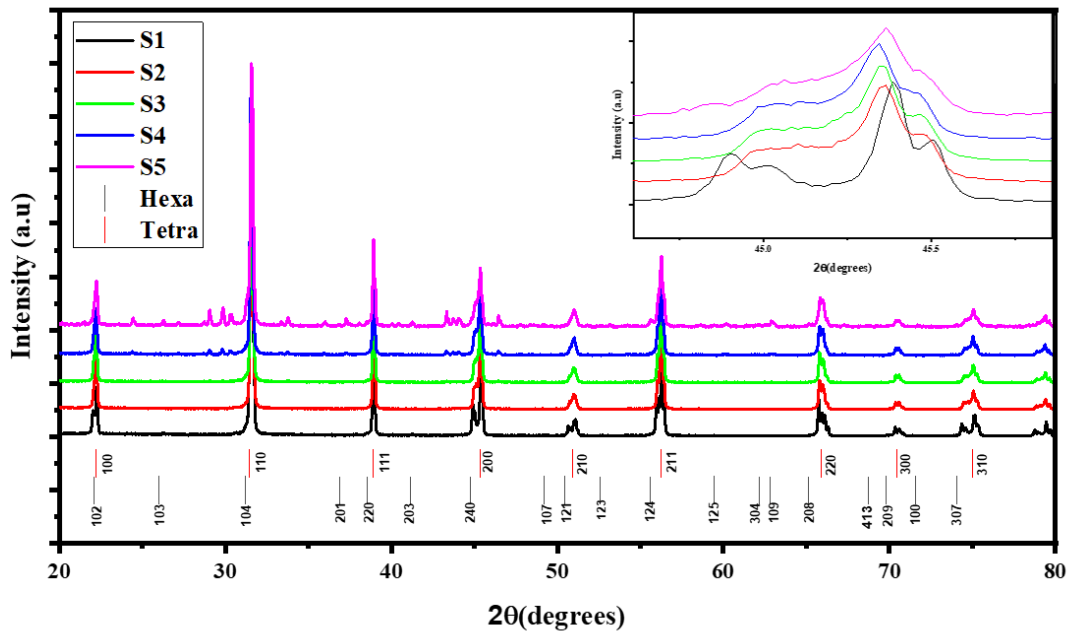


Fig 4.3: X-ray diffraction pattern for set of samples calcinated at 1200°C

From the XRD, the tetragonal phase has been confirmed. Also, the splitting of 45° peak shows high c/a ratio for the pure sample. However, for further investigations, Reitvald Refinement has been performed.

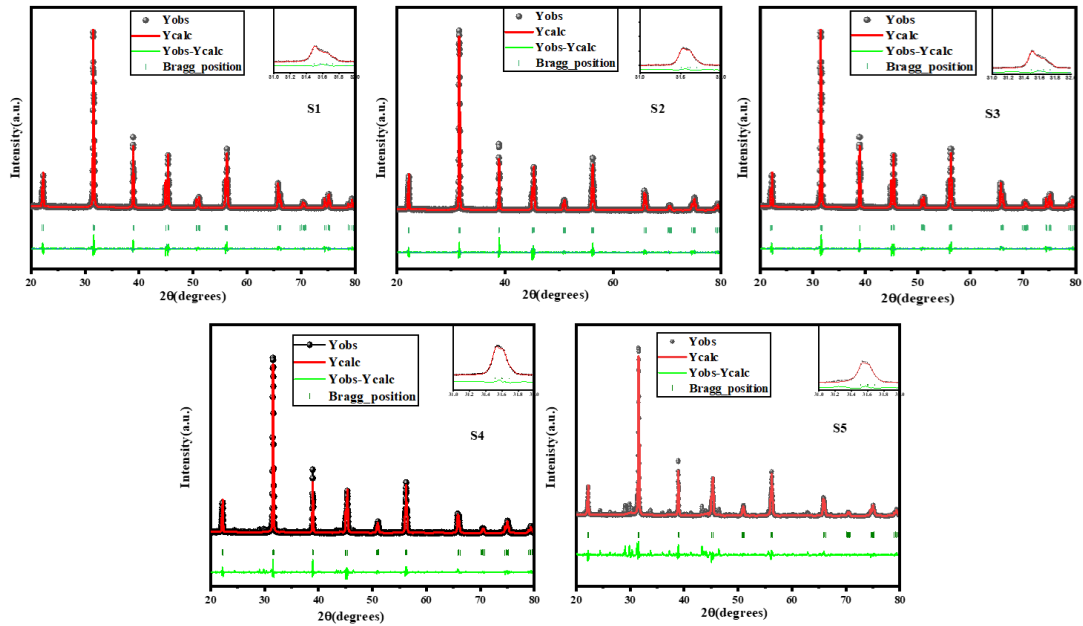


Fig 4.4: Reitvald Refinement of $\text{Ba}_{1-x}\text{Ni}_x\text{TiO}_3$ for $x=0, 0.03125, 0.0625, 0.125$ and 0.25

All the data has been refined such that the R_{wp} and R_p parameters are almost identical. And the fitting parameter χ^2 has been kept as low as possible. However, 25% doped one having more non-stoichiometry, thereby, making it difficult to fit properly.

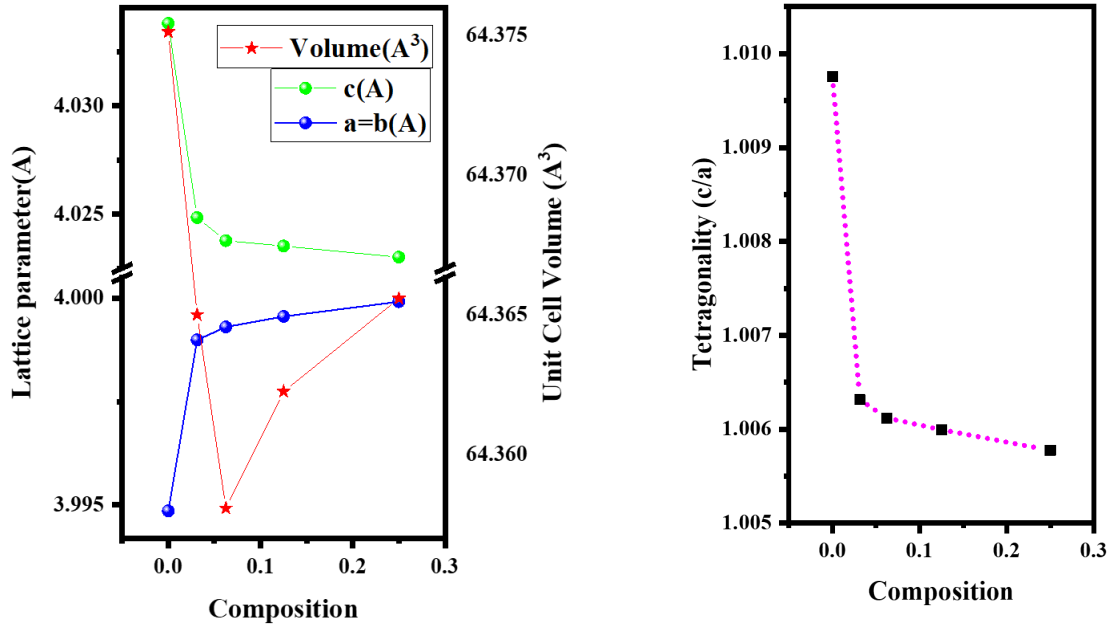


Fig 4.5: Lattice parameters, cell volume and Tetragonality variations with composition

As per the Fig 4.5, the tetragonality has been seen in the decreasing trend with increase in the substitution which indicates that the substitution more prefers the cubic phase. However the rate of change of a and c is different for every sets, hence making a minima of cell volume for S3 sample.

The Williamson-Hall (W-H) plot is a valuable tool for analyzing X-ray diffraction (XRD) data to determine both crystallite size and microstrain in a sample. It helps differentiate whether peak broadening at a specific diffraction angle arises from small crystallite size or strain within the material.

Microstrain develops in the structure due to various defects such as point defects, grain boundaries, and stacking faults. The W-H method accounts for these factors, providing a more accurate estimation of crystallite size while simultaneously assessing strain effects. Thus, peak broadening in XRD patterns offers critical insights into both crystallite size and internal strain[8].

The W-H plot is expressed as:

$$\beta \cos \theta = 4\epsilon \sin \theta + k\lambda/d \quad (4.1)$$

where $\beta \Rightarrow$ FWHM of peak at θ degree

$\epsilon \Rightarrow$ Microstrain in the sample

$\lambda \Rightarrow$ wavelength of x-ray

$d \Rightarrow$ crystallite size

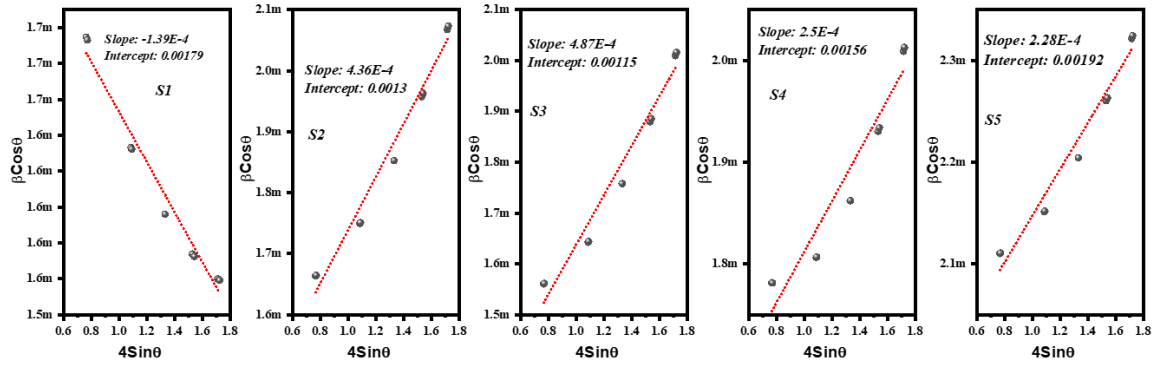


Fig 4.6: Fitting of williamson-hall plot from refined data

This slope and intercept have further used to investigate the crystallite size and microstrain.

The crystallite is assumed to be spherical in shape, thereby taking k equals 0.89 .

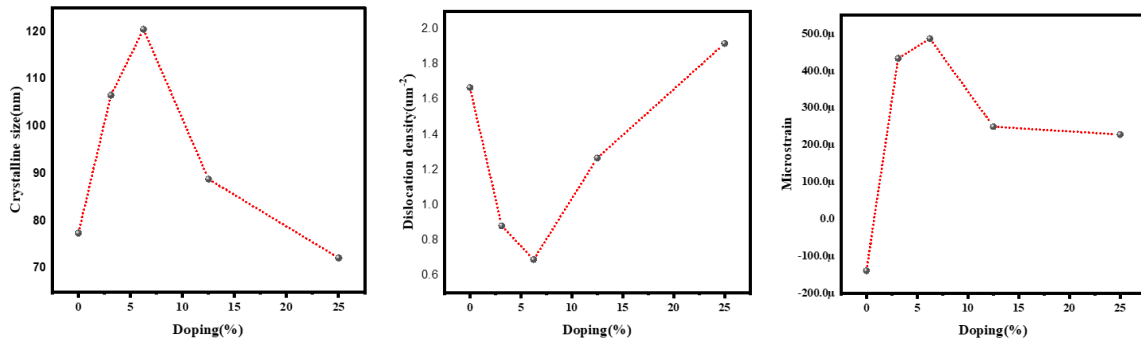


Fig 4.7: Variation of Crystallite size, dislocation density and microstrain with doping

For pure Barium Titanate, the strain has been observed as compressive in nature which means the crystal lattice is contracted due to internal stresses. When Nickel is introduced into the material, the microstrain shifts to a tensile nature, initially resulting in an increase in crystallite size. However, since the ionic radius of Nickel is smaller than that of Barium, this positive strain effect may be partially compensated by the size difference, ultimately leading to a further decrease in crystallite size. Dislocation density is a measure of the number of dislocations (defects in the crystal lattice) per unit area in a material and has been plotted above which is inversely proportional to the crystallite size of the sample.

4.3: Raman Analysis

Raman spectroscopy is known to be a very sensitive tool for obtaining information about changes in the local symmetry of the structure. Any small changes in structure due to doping should be reflected in the Raman spectra better than any other technique.

The Raman spectra of BTO powders reveal prominent peaks corresponding to the E (TO) phonon mode at $\sim 40\text{ cm}^{-1}$, an interference feature at $\sim 180\text{ cm}^{-1}$, a broad A₁ (TO) mode at 275 cm^{-1} , a combined sharp B₁ mode and E (TO + LO) mode at 307 cm^{-1} , a combined A₁ (TO) mode and E (TO) mode at $\sim 520\text{ cm}^{-1}$ and finally a combined A₁ (LO) and E (LO) mode at 717 cm^{-1} . The nearby A₁ (TO) and the E (TO) modes $\sim 520\text{ cm}^{-1}$ appear to be convoluted and appear as a broad asymmetric peak.

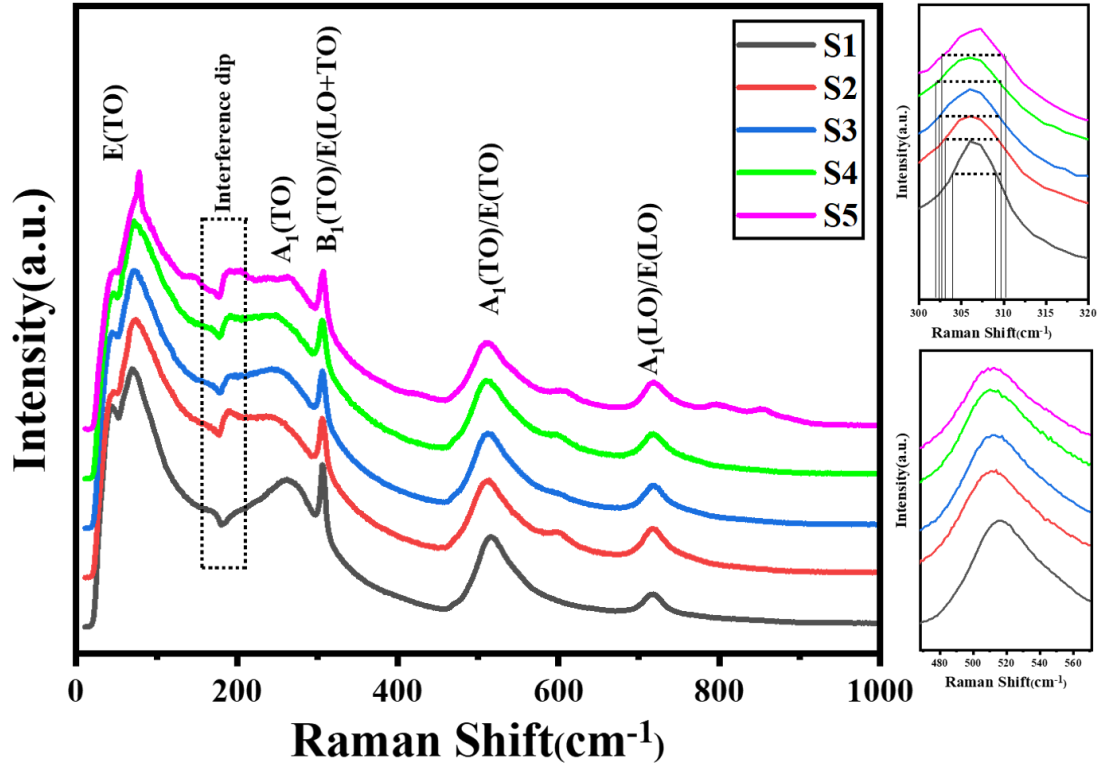


Fig 4.8: Raman spectra of Nickel modified Barium Titanate

$\text{Ba}_{1-x}\text{Ni}_x\text{TiO}_3$	E (TO)	A1 (TO)	B1(TO)/ E(LO/TO)	A1(TO)/ E(TO)	A1(LO)/ E(LO)
S1	43.33	262.18	306.03	514.9	717.37
S2	45.90	241	306.03	511.6	717.6
S3	44.63	249.5	306.03	511.6	717.6
S4	45.9	249.6	306.03	509.9	717.6
S5	47.22	262.7	307.29	509.16	717.6

Table 4.1: Raman shift for different vibrational modes

A sharp peak around 306 cm^{-1} (E(TO+LO)) is often known to be a characteristic peak of tetragonal phase and got merged with $A_1(\text{TO})$ peak at higher temperature. Thereby, cubic

Barium Titanate has a broad peak consist of the mixture of these two. From fig, we can see that as the doping is increasing, the sharp 306cm^{-1} peak is getting broader indicating the reducing nature of tetragonality with doping. $A_1(\text{TO})$ peak corresponds to the lattice vibrations involving Ti and O displacements (Ti-O bonds towards a and b lattice parameter). However, sharp peak linked to the ferroelectric nature of BaTiO_3 (Ti-O bending towards c-axis). Hence the ratio of intensity of both the peak could be proportional to c/a (tetragonality) ratio in the sample. And it is decreasing with doping, satisfying both the XRD data and broadness of E(TO) peak. The peaks at higher Raman shift (515 and 717 cm^{-1}) corresponds to $(\text{TiO}_6)^{2-}$ octahedra and from above Fig 4.8, we can see there is not much change in their FWHM and peak positions indicating that the dopant doesn't affected the B-site. However slight changes are due to affect of A-site on this octahedra [51][52].

A peak around 800cm^{-1} in S5 sample shows a presence of hexagonal nature [46] in it supporting the XRD data. Since 25% is not a small composition and the cationic size difference between Nickel and Barium is quite large, Ni starts to incorporate into the B-site and displaces the same size ion (i.e. Titanium). However, to maintain the stoichiometry, some impurities have been formed which can be seen in the XRD as well and predicted as BaTi_2O_5 .

A strong dip (known as interference dip) has been observed at 180cm^{-1} . The origin of this dip is claimed as the consequence of Fano resonance that arises due to the interference between a discrete quantum state and a continuum of states. Here, the sharp phonon peak corresponds to transition from a discrete quantum state, whereas the electronic band act as a continuum of states.

4.3.1: Temperature dependant Raman Spectroscopy

Since Barium Titanate phase transformation occurs nearby 373K , its interesting to see the behaviour of phonon mode evolution with temperature or nearby transition temperature. As per literature, $E(\text{TO}+\text{LO})$ (Ti-O bending towards c-axis) peak around 306cm^{-1} is responsible for the ferroelectricity in Barium Titanate. This mode appears to get softens when temperature is getting increased and vanished around the phase transition. The $A_1(\text{TO})$ peak corresponds to the lattice vibrations involving Ti and O displacements (Ti-O bonds towards a and b lattice parameter) merges to this E(TO) ferroelectric peak. Its obvious as the titanium starts acquiring

the centro-symmetric position, all a,b and c becomes equivalent and hence both the peak merges. As we know that this E(TO+LO) peak is responsible for the ferroelectricity, the degrading and softening of this peak will tell us about the degrading of tetragonal (ferroelectric) phase to cubic (paraelectric) phase.

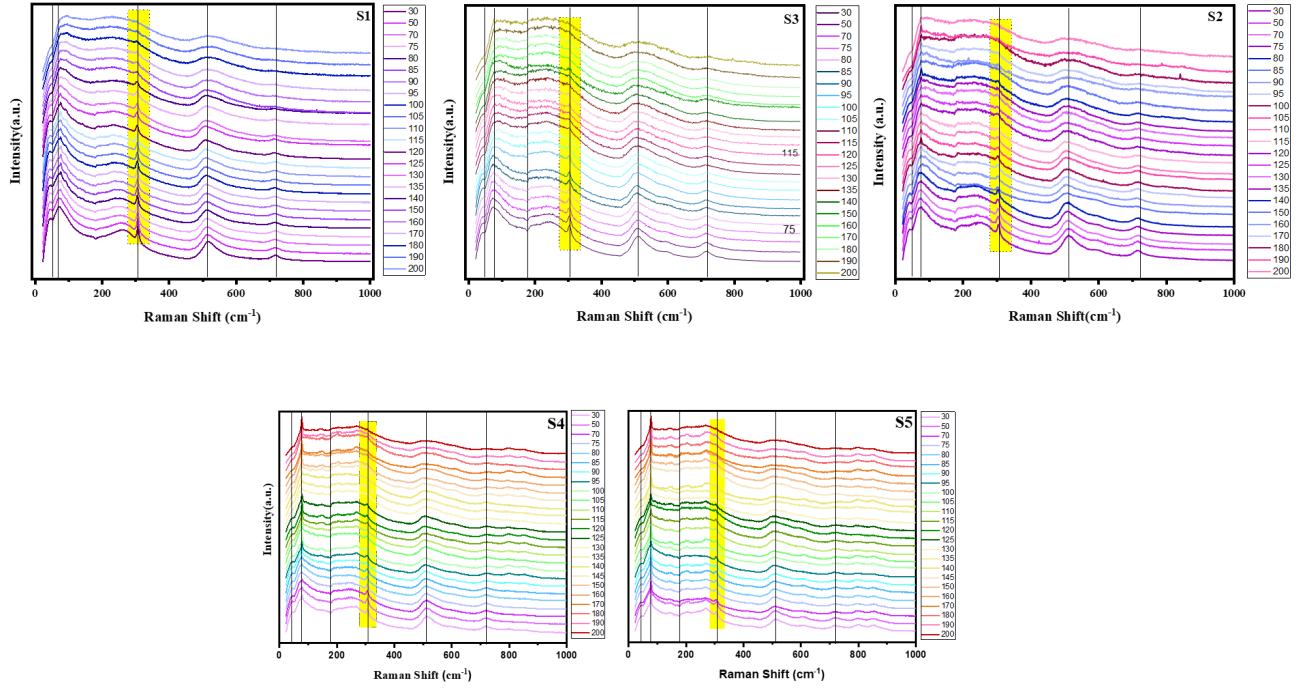


Fig 4.9: Temperature dependant Raman spectra of all samples

4.4: FTIR (Fourier transform Infrared Spectroscopy)

FTIR is one of the most sensitive technique to analyze the strength and type of chemical bond by measuring the lattice vibrations. The strong absorption bands were observed in the range $400\text{--}800\text{ cm}^{-1}$ and 2300 cm^{-1} .

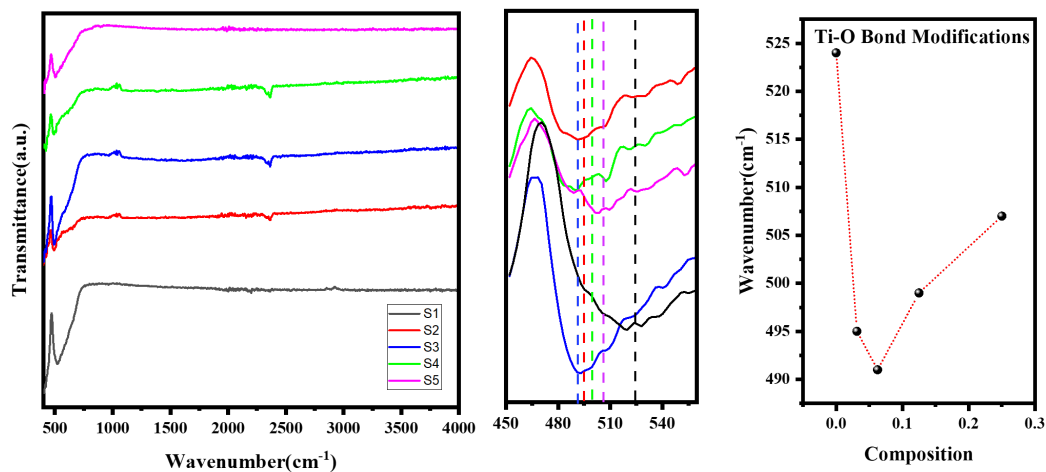


Fig 4.10: a. FTIR spectra of all samples b. Modifications in the wavenumber associated with Ti-O bond

The absorption peak located near 2320 cm^{-1} is attributed to CO_2 adsorbed on the surfaces of perovskite [40]. This could be explicated by considering a dipole–dipole interaction between the perovskite crystal and the polar CO_2 molecule.

A broad peak, around 530 cm^{-1} , is assigned to Ti–O stretching vibrations of TiO_6 octahedra.

In this mode, the direction of stretching is along with the spontaneous polarization with the tetragonal phase. From the Fig 4.10, we can see that the Ti-O bond stretching has a red shift first and then a blue shift. It means the presence of Ni^{2+} in place of Ba^{2+} drastically weakens the bond strength and then slowly strengthens, follows the trend of Crystallite size. A very small dip at 440 cm^{-1} tells us about the Ba-O bond, which widens with doping. Since the Ni-O bond stretching lies around 443 cm^{-1} [47], thereby its challenging to differentiate.

4.5: Band gap analysis

Optical absorption for the samples has been calculated using Diffuse Reflectance Spectroscopy (DRS). It is a technique that analyzes the spectral characteristics by measuring the light reflected from them, thereby very useful in performing the optical analysis of solid opaque samples. The assumption we used to take here is our sample is infinitely thick so that no light can transmit through it.

The absorbance can be calculated by the obtained Reflectance using the Kubelka-Munk function i.e,

$$F(R) = \frac{(1-R)^2}{2R} = \frac{K}{S} \quad (4.2)$$

K/S = Kubelka munk Function F(R)

And this K/S ratio is coined as a term equivalent to absorbance here i.e. α

The Kubelka Munk function has been plotted below. The point at which local maxima of absorbance occurs(around 400 nm), is considered to be the point of bandgap. Because at this point, maximum number of photons are getting absorbed. This bandgap is due to the transition of electron from 2p of oxygen to 3d orbital of Titanium. We also see some humps around 500 and 700 nm for all samples other than pure one. This shows the modification in band structure by the involvement of Nickel. At higher wavelengths, it has been observed that Charge transfer transition(Metal-Metal, Metal-Ligand, Ligand-Metal) lies in this energy range[48]. Hence, it is suspected to be any of them.

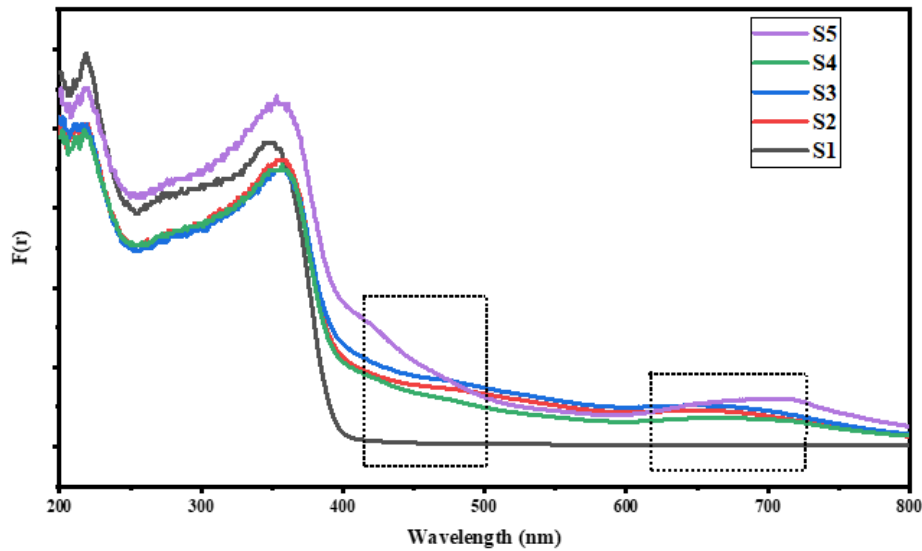


Fig 4.11: Absorbance spectra of all samples using DRS

This absorbance can be used to analyse the band-gap using Tauc-plot equations i.e,

$$(\alpha h\nu)^n = A(h\nu - E_g) \quad (4.3)$$

where,

$n \rightarrow$ Transition type ($n=2$ for direct and $\frac{1}{2}$ for indirect bandgap)

$E_g \rightarrow$ Band gap energy

$h\nu \rightarrow$ Photon energy

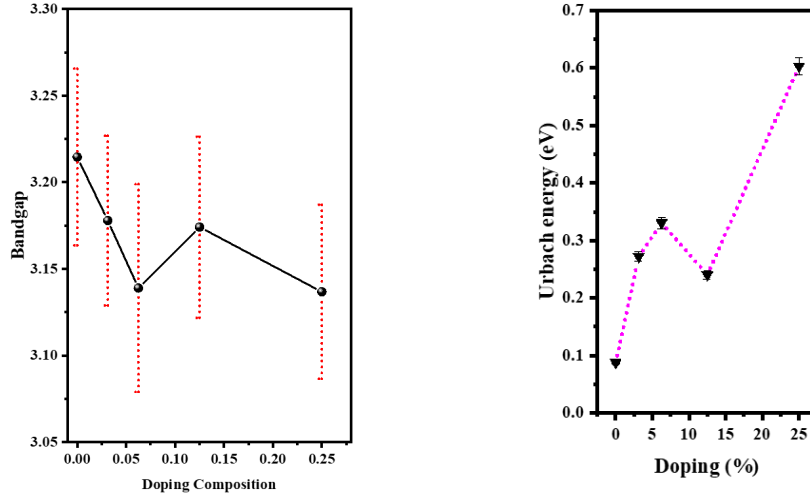


Fig 4.12: a) Bandgap variation with doping b) Urbach energy variation with doping

Since Barium Titanate has a direct Bandgap, we have taken $n=2$ for our calculations.

Due to the presence of defects and thermal agitations, a crystal structure can never be a perfect periodically arranged system. The disorder introduced due to different structural, thermal and compositional fatigues effectively modifies the local potential profile around the defects. This can lead to different shallow energy levels in the forbidden energy band-gap region. The tail states in general make the sharp transition of the absorption coefficient to be exponential growth near the fundamental absorption region. So, the extension of the tail can be parameterized as a measure of disorder, which is known as Urbach energy (E_U).

The Band gap is seen to be decreasing by an order of 10^{-2} . Along with that, Urbach energy E_U is increasing drastically with the substitution of Nickel, caused by lattice distortion.

4.6: Field Emission Scanning electron microscopy (FE-SEM)

Field Emission Scanning Electron Microscopy (FESEM) operates by scanning a sample surface with a high-energy electron beam in a raster pattern. The interaction between the electrons and the sample's atoms generates various signals that provide detailed information about the surface

topography, composition, and electrical conductivity of the material. This technique enables high-resolution imaging, making it a powerful tool for analyzing nanostructures and fine surface details.

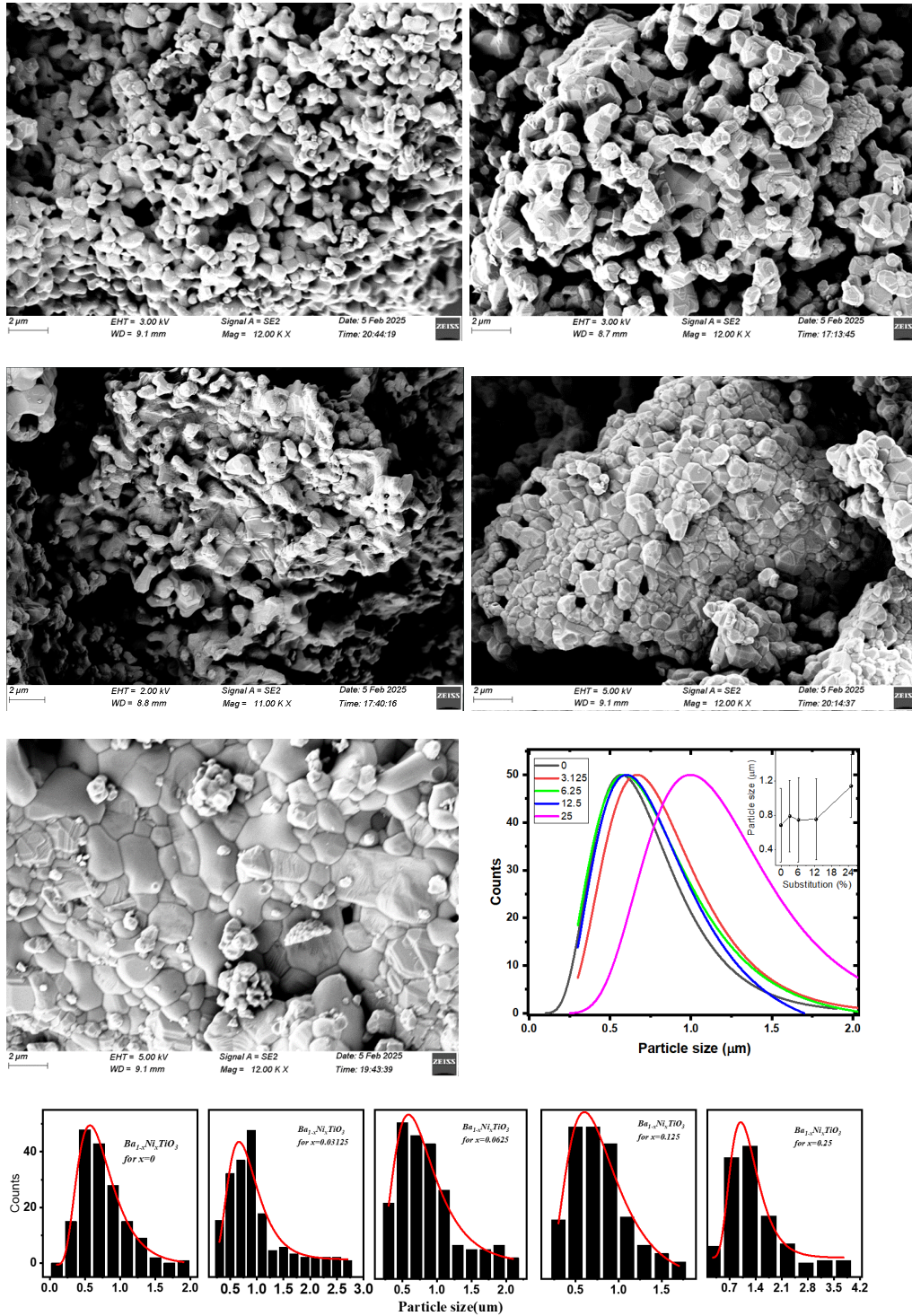


Fig 4.13: Morphology of all samples and particle size variation with doping

The SEM images above depict the morphology of the particles, revealing an asymmetric particle size distribution. Due to this asymmetry, a log-normal function is used to determine the average particle size, rather than a Gaussian function, which assumes a symmetric distribution. The log-normal distribution provides a more accurate representation of the particle size variation in the sample.

The pure Barium Titanate sample exhibits the smallest particle size, which increases progressively with Ni incorporation. Notably, the particle size nearly doubles when 25% Nickel is substituted. The variation in particle size from its mean value has been analyzed and plotted above, providing insights into the impact of Nickel doping on grain growth and overall morphology.

4.7: Dielectric Spectroscopy

Dielectric materials are basically insulating materials; however, calling them insulators doesn't meet the context here. Rather than conducting charge, they store energy in electrical form, indicating their charge-storing capability. In dielectric materials, charge is not entirely free to move. When exposed to an external electric field, the material undergoes polarization, aligning in the opposite direction of the applied field. This polarization generates an opposing electric field within the material, effectively reducing the overall internal electric field.

In this study, a broadband dielectric spectrometer (Newton's 4th Ltd.) was used to perform dielectric measurements over a frequency range of 100 Hz to 1 MHz.

The fundamental working principle of this impedance analyzer is based on the Wheatstone bridge configuration, where the material under investigation is placed alongside three known capacitances to determine its dielectric response accurately.

The capacitance has been measured using this principle and then using the relation:

$$\varepsilon'(\omega) = C_p d / \varepsilon_0 A \quad (4.4)$$

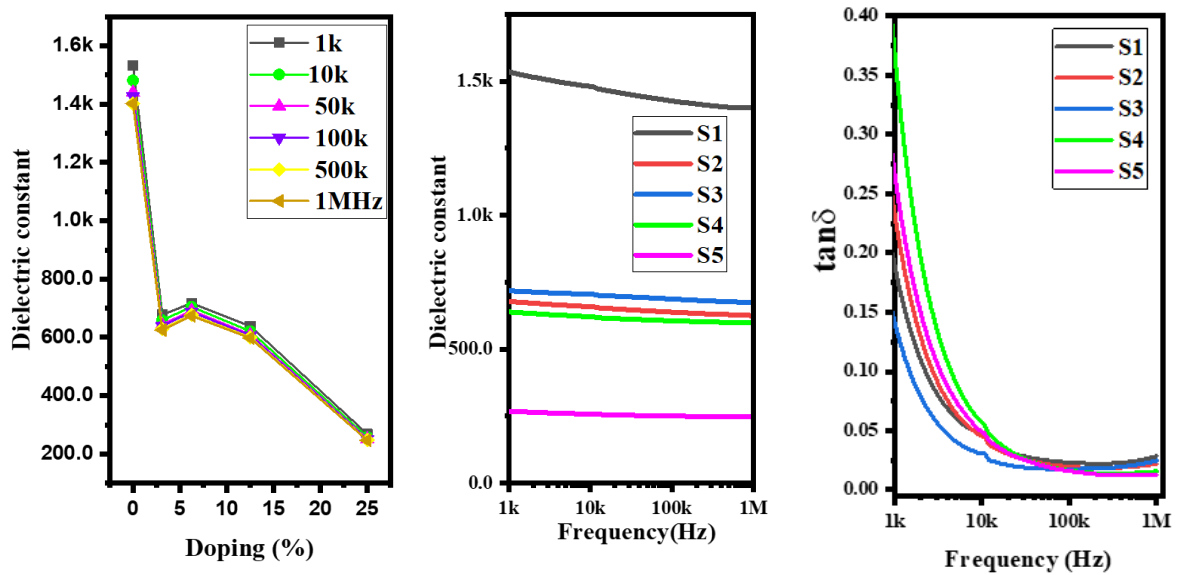


Fig4.14: Variation of Dielectric constant and $\tan\delta$ at room temperature

The pure Barium Titanate shows a very high dielectric constant at room temperature.. With the incorporation of Ni in the BTO lattice, there is a change of the lattice composition, which seems to reduce ϵ_r drastically. The tetragonality is seen to be decreasing with the involvement of Nickel, and so as the dipole moment, which further affects the dielectric constant here. The ϵ_r of the samples depends mainly on four different contributions i.e., Ionic polarization includes space charge and interface polarization (ϵ_i), dipolar polarization (ϵ_d), atomic polarization (ϵ_a), and electronic polarization (ϵ_e).

The $\tan\delta$ decreases considerably with increase of frequency, minimised around 200KHz, and then increases. The loss factor is found to be maximum for Pure BTO and decreases for samples S2, S3, S4 and S5 respectively. This can also be seen via AC conductivity and IV plots.

4.7.2: Temperature dependent Dielectric constant Analysis

To investigate about the curie temperature, temp dependent dielectric constant have been measured. From literature, the phase transition from ferroelectric to paraelectric is found to be near 120° C. However substituting Nickel into the A-site has give us transitions as different temperature as plotted below.

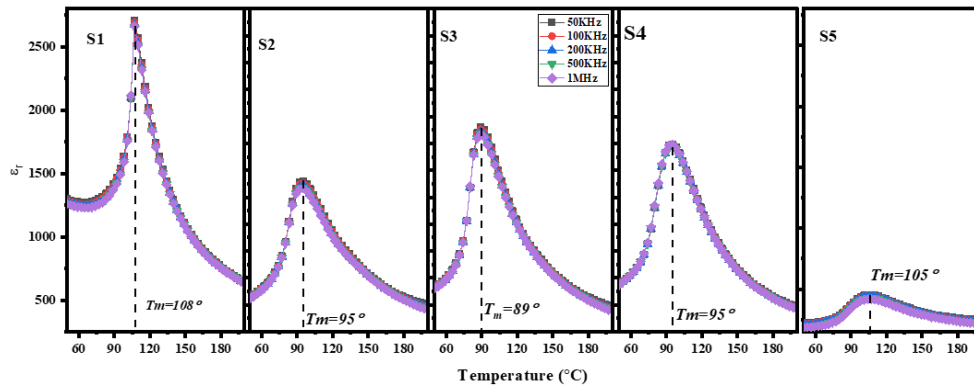


Fig 4.15: Temperature dependence of Dielectric constant

The phase transition temperature exhibits a sharp decline up to 6% Nickel doping (sample S3). However, with further Nickel substitution, the transition temperature begins to rise, with sample S5 displaying a value nearly identical to that of the undoped (pure) sample. This trend may be attributed to variations in the crystallite size within this set of samples.

A key distinction between the pure and doped samples lies in the increased diffuseness of the phase transition, which is attributed to the incorporation of Nickel. As the Nickel content increases, the transition becomes progressively broader, with this broadening evident on both sides of the transition peak. Such broadening is likely the result of local structural heterogeneities within the crystal lattice.

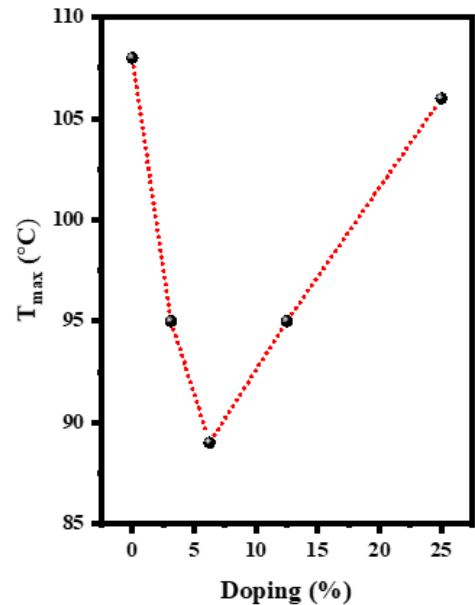


Fig 4.16: Curie Temperature variation with doping

The presence of Nickel influences the activation energy of the ferroelectric domains. Domains in which Nickel substitutes Barium, may exhibit different Curie temperatures (T_c) compared to neighboring domains, resulting in a distribution of T_c values throughout the material. Consequently, the energy required to destabilize each domain varies, leading to a diffuse and

broadened phase transition rather than a sharp one. This broadening and diffuseness are indicative of structural disorder and are strongly correlated with the Urbach energy.

As a result, the temperature corresponding to the maximum dielectric constant (T_m) cannot be regarded as the precise point at which the material fully transit into the paraelectric phase. Instead, the onset of the paraelectric phase can be identified by the temperature at which the material begins to obey the Curie law. This specific temperature is referred to as the deviation temperature (T_{dev}). To determine this, a plot of the inverse dielectric constant ($1/\epsilon$) versus temperature was generated.

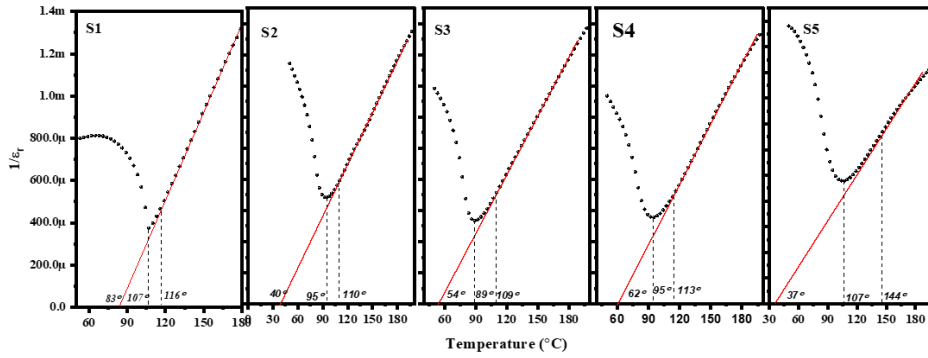


Fig 4.17: Plot of inverse of epsilon with temperature

The difference between T_{dev} and T_m has been analyzed and plotted. This deviation reflects the extent to which the dielectric response diverges from ideal Curie law behavior. It provides insight into the degree of diffuseness present even after the apparent disappearance of ferroelectric domains. The temperature gap indicates the additional thermal energy required for the complete transition to the paraelectric phase. This suggests that, despite significant thermal excitation, strong dipole–dipole interactions may still persist, necessitating even higher temperatures for their complete disruption.

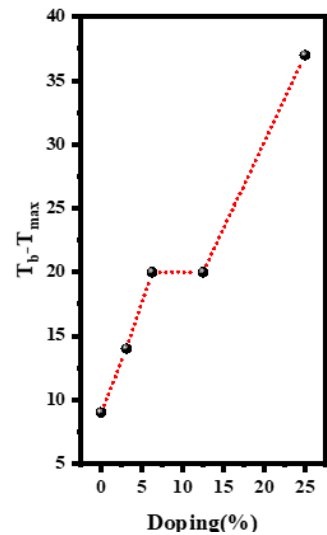


Fig 4.18: Deviation between T_m and T_b

Diffuseness measurement using Modified Curie weiss law

Since the sample is found to be having the diffused phase transition. It used to follow the modified curie-weiss law (often known as Uchino's law). Modified law can be written as

$$\ln\left[\left(\frac{\epsilon_{\max}}{\epsilon_r}\right) - 1\right] = \gamma \ln[T - T_m] - 2\ln(\sqrt{2}\delta) \quad (4.5)$$

A straight line is fitted in the paraelectric phase near the transition between $\ln[T - T_m]$ and $\ln[(\epsilon_{\max}/\epsilon_r)-1]$ in the paraelectric phase i.e. in the $[>T_m]$ region.

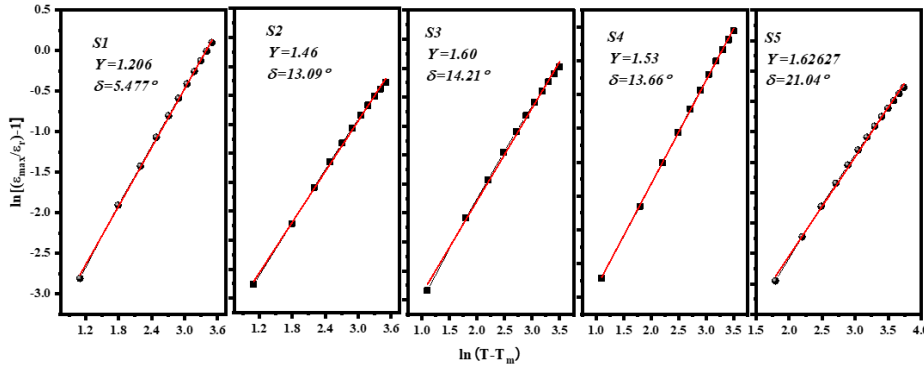


Fig 4.19: Fitting of Modified Curie-Weiss law

From the above graph, two key parameters can be extracted: one is γ (gamma) and the other is δ (delta). Among these, δ is considered to hold more physical significance in characterizing diffuseness, whereas γ is primarily a fitting parameter without direct physical interpretation.

According to theoretical models, a diffuse phase transition (DPT) lies between the behavior of normal and relaxor ferroelectrics. Uchino proposed that the value of γ should lie between 1 and 2. On the other hand, δ represents the degree of peak broadening or the extent of temperature dispersion in a DPT. A higher value of δ indicates greater broadening of the dielectric peak, which can be directly correlated to the level of structural disorder within the material.

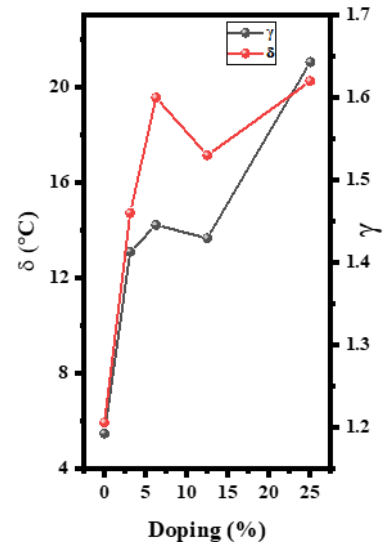


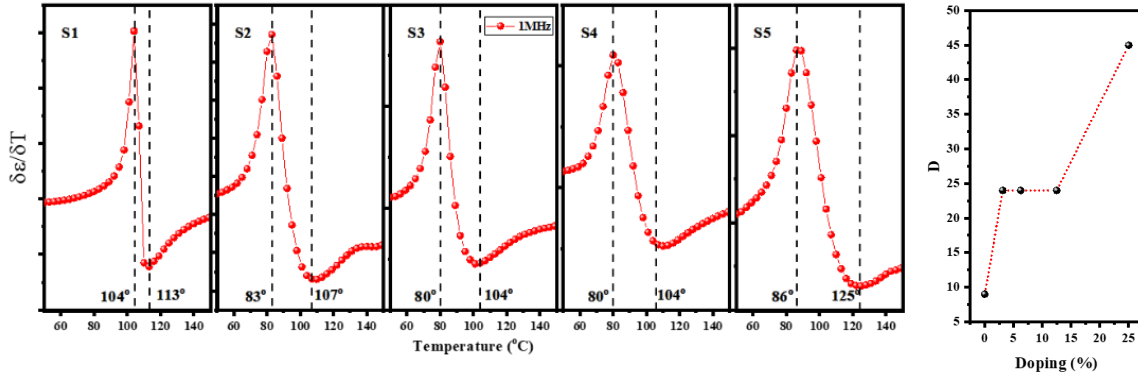
Fig 4.20: Variation of γ and δ with doping

Both parameters, γ and δ , increase with the substitution of Nickel in the sample. The rise in γ suggests a shift in the material's behavior toward a more relaxor-like nature, indicating the potential emergence of frequency dependence in the Curie temperature with further doping. Meanwhile, the increase in the δ parameter reflects a growing degree of structural disorder introduced by Nickel substitution. As the doping level increases, lattice disorder becomes more pronounced, resulting in broader dielectric peaks and enhanced diffuseness in the phase transition.

Uchino's law for diffuseness

To estimate the diffuseness, Uchino advised to plot the derivative of ϵ_r with temperature and the difference between maxima and minima value will estimate the value of diffuseness [49].

$$D = \left(\frac{\partial \epsilon}{\partial T} \right)_{min} - \left(\frac{\partial \epsilon}{\partial T} \right)_{max} \quad (4.5)$$



Therefore, the derivative has been plotted to extract the D parameter. This approach offers greater precision as it accounts for the broadening in both the ferroelectric and paraelectric regions. As expected, the diffuseness was observed to increase with doping.

Temperature dependant Bode's Plot

Relaxation time can be evaluated through equivalent circuit analysis using Cole–Cole plots. The Cole–Cole plots of the samples under investigation exhibit a single semicircle, suggesting the presence of only one dominant relaxation process. This also implies minimal or negligible contribution from grain boundaries. Therefore, the data can be accurately modeled using a

single RC circuit. Accordingly, relaxation time can be determined using the Bode plot method (as described in Chapter 2), where the frequency at which the imaginary part of impedance (Z'') reaches its maximum corresponds to the relaxation frequency.

$2\pi fRC=1$ where RC is considered as the relaxation time.

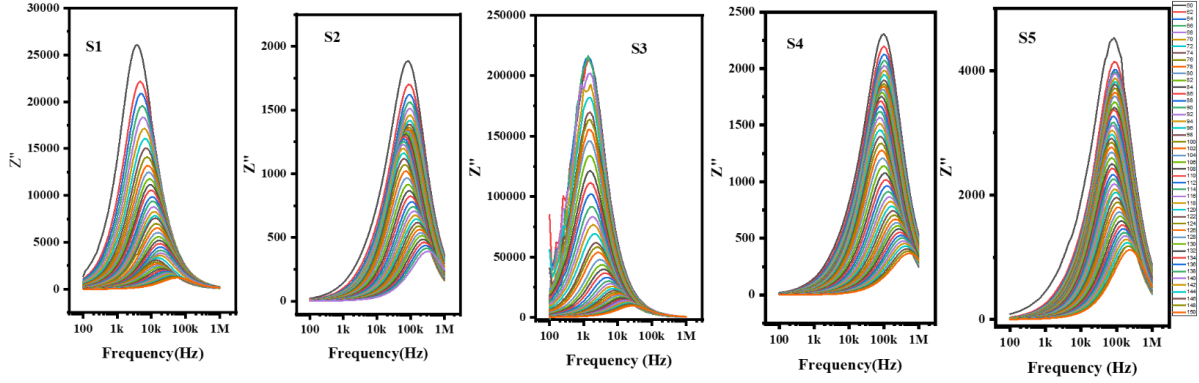


Fig 4.21: Bode's plot from Temperature range (50°-140°C)

From the above plots, a clear shift in the frequency corresponding to the maximum imaginary part of impedance (Z'') can be observed. The general trend indicates that frequency decreases with increasing temperature. This implies that as thermal energy increases, the relaxation frequency decreases, resulting in shorter relaxation times. Consequently, at higher temperatures, the time required for the domains to align with the applied electric field is reduced.

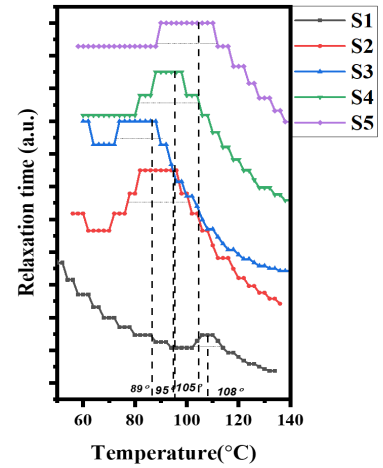


Fig 4.22: Variation of relaxation time with Temperature

However, near the phase transition region, a noticeable hump appears, indicating a deviation in the relaxation time behavior. Around the phase transition, the sample's response time to the

electric field diverges from the established trend. In the pure sample, this shift is sharp, whereas in doped samples—where diffuseness has been introduced—a broadening of this shift is also evident. This is expected, as the incorporation of Nickel induces lattice disorder, leading to the formation of diverse local structural environments, each with its own relaxation time. These experimental findings are in strong agreement with the earlier observations regarding disorder and diffuseness.

Ac conductivity

AC conductivity can be calculated using single Power law defined by

$$\sigma_{AC}(\omega) = \sigma_{DC} + A\omega^n \quad (4.6)$$

Where $\sigma_{AC}(\omega)$: Total AC conductivity at angular frequency ω

σ_{DC} : DC conductivity

A: Temperature-dependent constant

ω : Angular frequency of the applied AC field

n: Power law exponent ($0 < s < 1$, typically)

Also, as derived earlier (in CH-3)

$$\sigma_{AC} = \omega\epsilon_0\epsilon''(\omega) \quad (4.7)$$

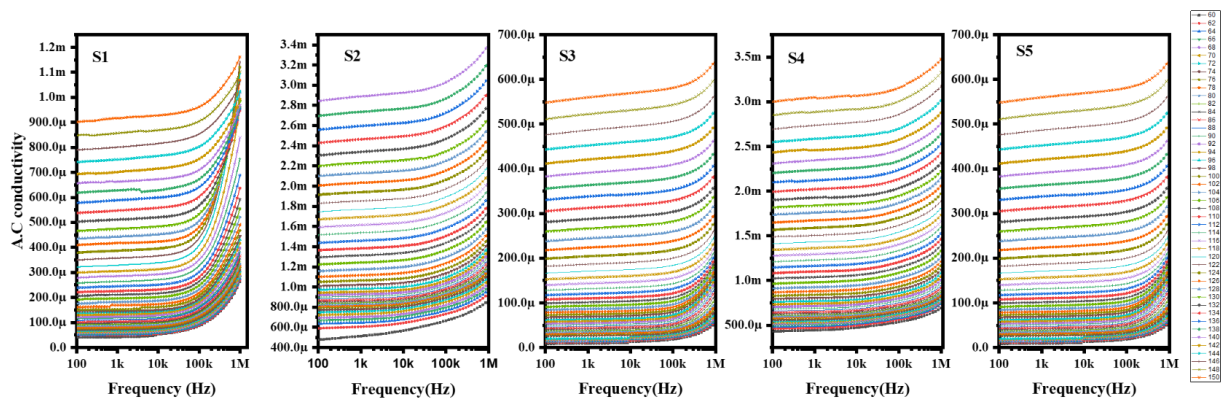


Fig 4.23: Temperature dependant AC conductivity plot for all samples

The AC conductivity has been calculated and plotted. The graph shows an initial region where the conductivity remains nearly constant, followed by an exponential increase at higher

frequencies. This behavior has been well described using a single power law model, from which both the DC conductivity and the power law exponent were extracted. However, at elevated temperatures, the influence of electrode polarization becomes more prominent, leading to slight deviations between the fitted curve and the actual data.

Since Barium Titanate behaves as a semiconductor, its DC conductivity increases exponentially with temperature. According to the Arrhenius relation:

$$\sigma_{dc} = \sigma_o \exp\left(\frac{-E_a}{K_b T}\right) \quad (4.8)$$

Here, E_a represents the activation energy required for charge carriers to move freely within the crystal lattice. A lower activation energy indicates that charge transport occurs more easily, corresponding to higher conductivity.

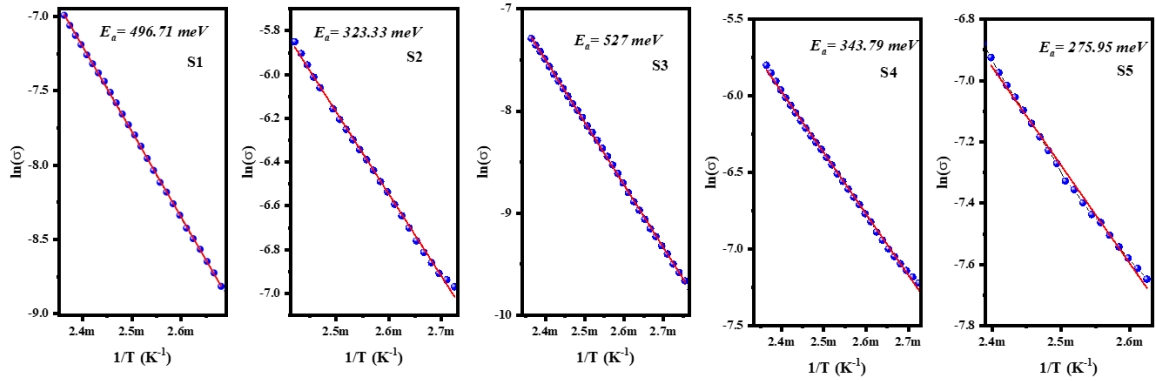


Fig 4.24: Fitting of Arrhenius relation in DC conductivity

The activation energy, calculated using the Arrhenius equation, is found to be in the range of hundreds of meV. In contrast, the thermal energy at room temperature is approximately 25 meV, which is significantly lower. As a result of this relatively high activation energy, the DC conductivity remains very low, since the likelihood of charge carriers overcoming or tunneling through such an energy barrier is minimal. With doping, the activation energy is found to be maximum for S3 sample followed by the S1, S2, S4 and S5 respectively.

The variation of n with temperature has been observed and plotted for both pure and doped samples. The transport mechanism is found to be a bit different in both the cases.

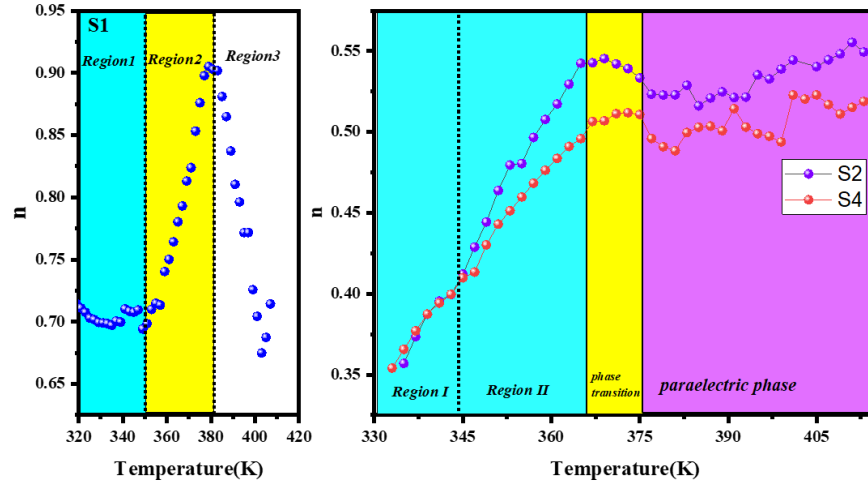


Fig 4.25: Variation of exponential parameter with temperature

In the undoped (pure) sample, the frequency exponent n initially remains nearly constant with temperature, around 0.7, indicating quantum tunneling as the dominant conduction mechanism. However, as the temperature increases, n rises significantly, reaching a maximum near the phase transition temperature (T_m). This behavior of n remains somewhat inconclusive in this region. Beyond the phase transition, in the paraelectric phase, the behavior aligns well with the Correlated Barrier Hopping (CBH) model.

In contrast, for the doped sample, the region before the phase transition is best described by the Non-Overlapping Small Polaron Tunneling (NSPT) model. Interestingly, two distinct energy barriers are observed, corresponding to different conduction processes, which become evident well before the phase transition. Around the transition temperature, the value of n remains stable, and beyond that point, no clear trend is observed, likely due to the influence of excessive thermal energy disrupting regular transport behavior.

CHAPTER 5 Future Aspects and Conclusion

Nickel-doped Barium Titanate ($\text{Ba}_{1-x}\text{Ni}_x\text{TiO}_3$, where $x = 0, 0.03125, 0.0625, 0.125$, and 0.25) was synthesized via the sol-gel method. The synthesized samples were calcined at temperatures of 900°C , 1000°C , 1100°C , 1200°C , and 1300°C . A secondary, non-stoichiometric phase, likely BaTi_2O_5 , was identified within the samples. The presence of this non-stoichiometric phase, along with the hexagonal phase, was found to be minimized at approximately 1200°C . Phase confirmation was achieved through X-ray diffraction (XRD) and Raman spectroscopy. Fourier-transform infrared (FTIR) spectroscopy revealed modifications in the Ti–O bonding environment upon Nickel doping. Diffuse reflectance spectroscopy (DRS) was employed to calculate Urbach energy, providing insight into the degree of lattice disorder. Scanning Electron Microscopy (SEM) was used to investigate the surface morphology and particle size of the samples. Dielectric spectroscopy revealed that the undoped sample exhibits a sharp ferroelectric-to-paraelectric phase transition, while the Nickel-doped samples show a more diffuse (broadened) phase transition. The degree of diffuseness was quantified using various theoretical models. Additionally, a broadening in the relaxation time peak near the phase transition was observed in the doped samples. AC conductivity measurements were analyzed using a single power law, and the temperature dependence of the exponent n indicated the presence of different charge transport mechanisms across various temperature regimes for the undoped and doped samples.

Future Aspects:

□ **Correlation between Diffuseness and Urbach energy:** The diffuseness observed around the phase transition reflects the broadening of the transition temperature, which arises from a distribution of Curie temperatures (T_c) associated with various local polar regions within the material. These regions require different activation energies to transition from the ferroelectric to the paraelectric phase, a variation caused by the lattice disorder introduced through doping. Similarly, Urbach energy represents the extent of the tailing near the optical

absorption edge, which also results from disorder in the lattice due to doping. Since both diffuseness and Urbach energy originate from the same underlying cause—structural disorder—there may be a significant correlation between these two physical parameters.

□ **Correlation between Fano asymmetry parameter and Diffuseness:** According to the literature, Barium Titanate exhibits a characteristic Fano interference dip around 180 cm^{-1} . This dip arises from the interaction between a sharp phonon mode and an electronic continuum, a phenomenon that is highly sensitive to structural disorder. Given that this effect also stems from the same fundamental origin—lattice disorder—it is plausible that the Fano asymmetry parameter may be correlated with the broadening observed in the diffuse phase transition.

CHAPTER 6 Extra works

Evolution of multiple phases in Ni-doped Barium Titanate in XRD with sintering Temperature.

a. By using XRD

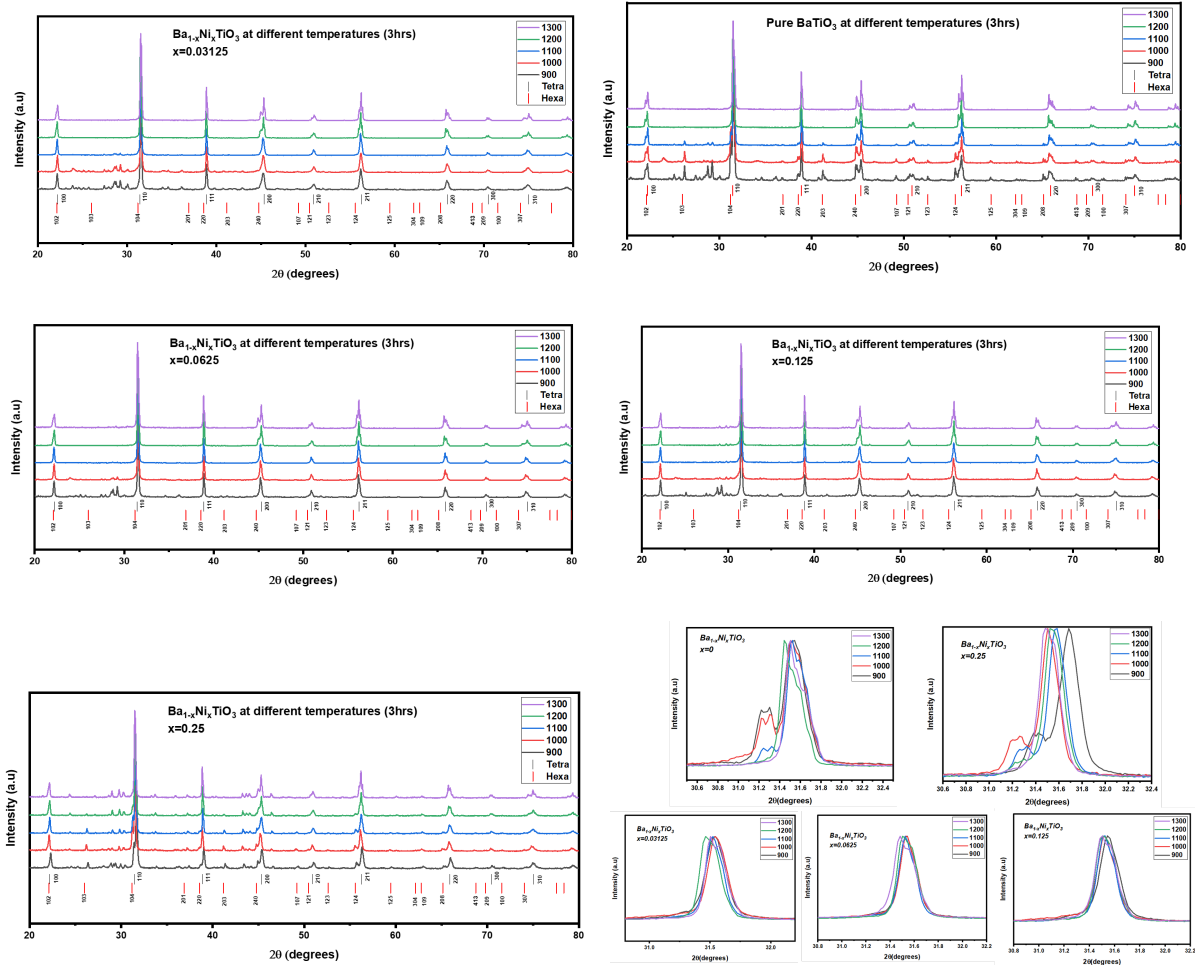


Fig 6.1: XRD of all the samples and evolution of 31° peak for each doping at different calcinating temperatures

From Fig 6.1, It can be seen that at lower temperatures, the material is present in the mixed state of both P4mm tetragonal and P63/mmc phase which ultimately leads to pure tetragonal phase at 1200oC. Also increase in doping concentration leads to a lower phase-forming temperature of the tetragonal phase. Splitting of the 31o peak is characteristic of the tetragonal phase. However that splitting almost vanished in 3.125%, 6.25%, and 12.5% samples signifies

the decrease in tetragonality. However pure and 25% set of samples have one more peak convoluted at 310 which represents the hexagonality in the structure and decays with an increase in calcinating temperature. The analysis of the percentage of hexagonality and tetragonality has been analyzed and plotted above. The hexagonal percentage fell sharply with the introduction of Nickel, reaching a 11 minima around 6%. However, a slight increase in hexagonality was observed after that, and a considerable amount of P63/mmc phase was present in 25%.

Along with that, an anomalous peak of a non-stoichiometric compound has also been observed having peaks around (27°-29°). After going through the literature survey, the compound was likely to be Ba_2TiO_5 , which finds minima while calcinating the sample. To remove the non- stoichiometric compound, its intensity with different doping and heat treatments was measured. It has been observed that the extra peaks vanished around 1100°-1200° C in all the samples except the 25% doped one. However, a further increase in temperature again leads to the presence of unwanted compounds.

b. By using Vibrational Raman spectroscopy

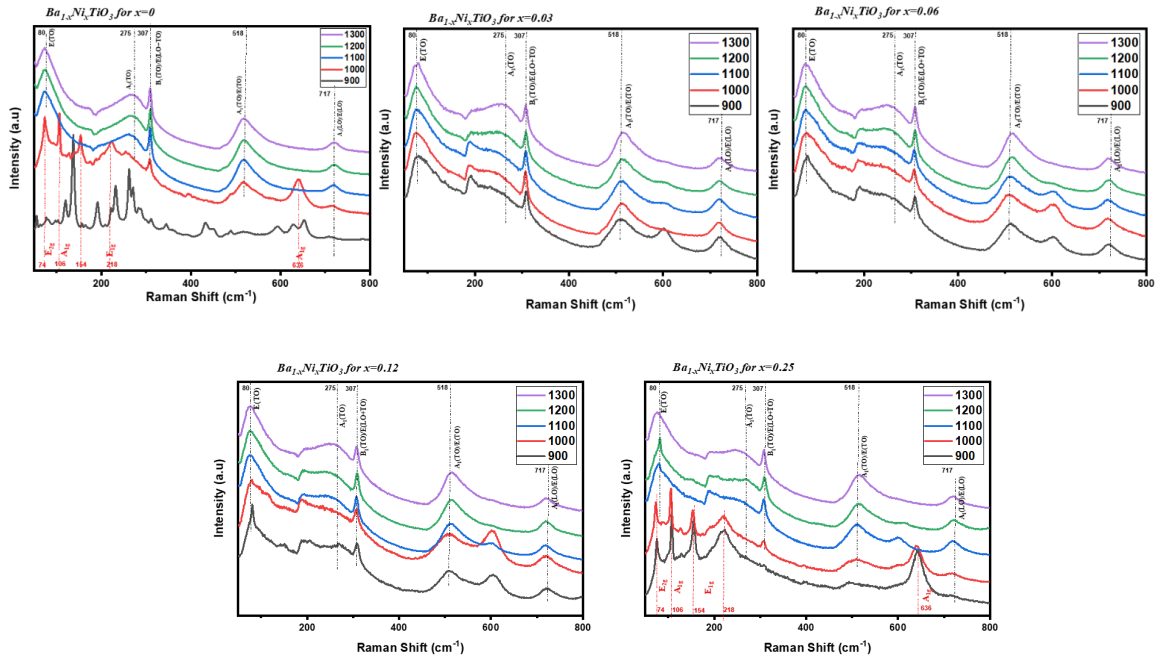


Fig 6.2: Evolution of Raman spectra for each samples at different calcinating temperature

In the undoped (pure) sample, the initial temperature-dependent data display multiple peaks, indicating the absence of a well-defined phase and the coexistence of both tetragonal and hexagonal structures. As the temperature increases, the Gibbs free energy reaches a minimum corresponding to the P4mm tetragonal phase, resulting in a complete phase transformation by 1200°C. In contrast, the 3%, 6%, and 12% Ni-doped samples exhibit a stable tetragonal phase as early as 900°C. However, the 25% Ni-doped sample shows a preference for the hexagonal phase at lower temperatures due to excessive Nickel content, eventually stabilizing entirely in this phase.

In the Fig 6.2, the black dotted lines represent the calculated phonon modes of the P4mm (tetragonal) phase, while the red lines correspond to those of the hexagonal phase. These phonon mode assignments are consistent with the XRD results discussed above.

Investigation of non-stoichiometric compound

An anomalous peak of a non-stoichiometric compound has also been observed having peaks around (27°-29°). After going through the literature survey, the compound was likely to be Ba_2TiO_5 , which finds minima while calcinating the sample. To remove the non-stoichiometric compound, its intensity with different doping and heat treatments was measured. It has been observed that the extra peaks vanished around 1100°-1200°C in all the samples except the 25% doped one. However, a further increase in temperature again leads to the presence of unwanted compounds.

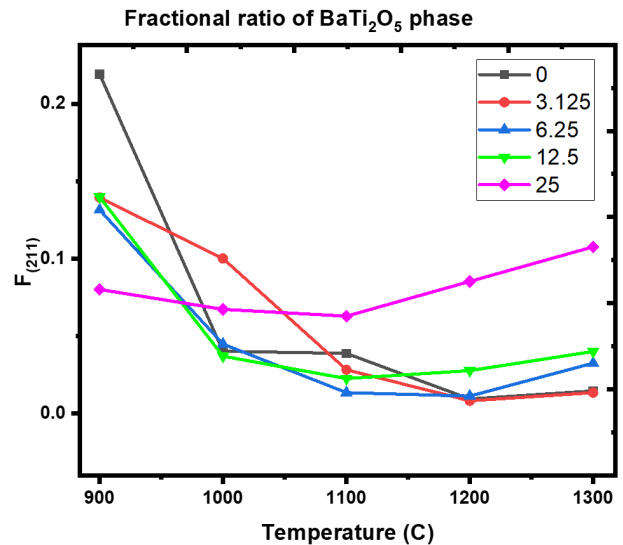


Fig 6.3: Variation of non-stoichiometry with doping

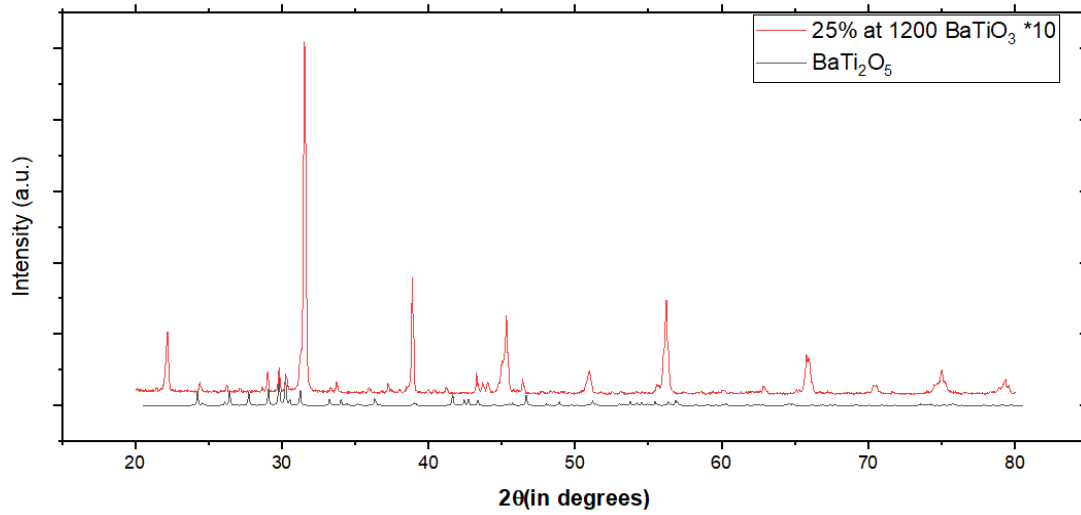


Fig 6.4: XRD peaks for BaTi_2O_5 and BaTiO_3

The non-stoichiometric compound Ba_2TiO_5 exhibits a diffraction peak that aligns precisely with the observed impurity peak as shown above. However, due to the presence of multiple possible secondary phases with overlapping peak positions in this region, a definitive phase identification cannot be made solely on this basis.

Fano Resonance in Barium Titanate

Fano resonance here in Raman Spectroscopy arises due to the interference between a discrete quantum state and a continuum of states.

Mathematically the Fano expression looks like,

$$I(\omega) = I_0 \frac{(q+\epsilon)^2}{1+\epsilon^2} \quad (6.1)$$

$I(\omega)$ is the intensity as a function of frequency ω .

I_0 is a scaling factor.

q is the **Fano asymmetry parameter**, which determines the shape of the resonance:

$q \rightarrow 0 \rightarrow$ anti resonant (symmetric dip-like): $q \rightarrow \infty \rightarrow$ Lorentzian resonance (symmetric peak).

Intermediate q values \rightarrow asymmetric peak.

E is the reduced energy parameter, given by:

$$\epsilon = \frac{\omega - \omega_0}{\Gamma} \quad (6.2)$$

where, ω_0 is the resonance frequency and Γ is the resonance width (damping factor).

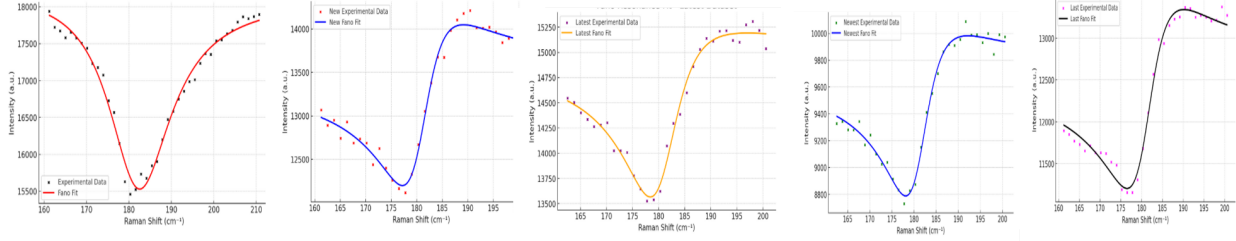


Fig 6.5: Fitting of Fano equation at 180 cm⁻¹ interference dip in BaTiO₃

Samples	q (Fano asymmetry parameter)	ω_0 (Resonance Frequency) cm ⁻¹	Γ (Resonance width) cm ⁻¹
S1	-0.0739	181.89	8.95
S2	0.666	180.86	11.05
S3	0.39	180.82	6.26
S4	0.53	181.19	5.82
S5	0.71	181.08	6.47

Table 6.1: Fitting parameters of fano equation

The fano curve has been fitted for the set of samples and the parameters has been extracted. The resonating frequency is same for all which is obvious, as the phonon peak doesn't depend on the structure(as it is discrete), but since the electronic band structure gets affected by doping, the interference gets affected. That impact leads to asymmetry in the curve and can be determined using asymmetry fano parameter. This parameter can be directly linked to the disorder in the lattice or in the band structure. In pure Barium Titanate, the value of q is almost 0 representing the symmetric dip.

BH Hysteresis loop Analysis

Since Nickel has been doped into the sample, it is possible that it may induce magnetic behavior within the lattice. However, achieving long-range magnetic ordering through A-site doping is generally challenging. To investigate this possibility, a B-H hysteresis loop was measured using a Vibrating Sample Magnetometer (VSM), and the results are presented below.

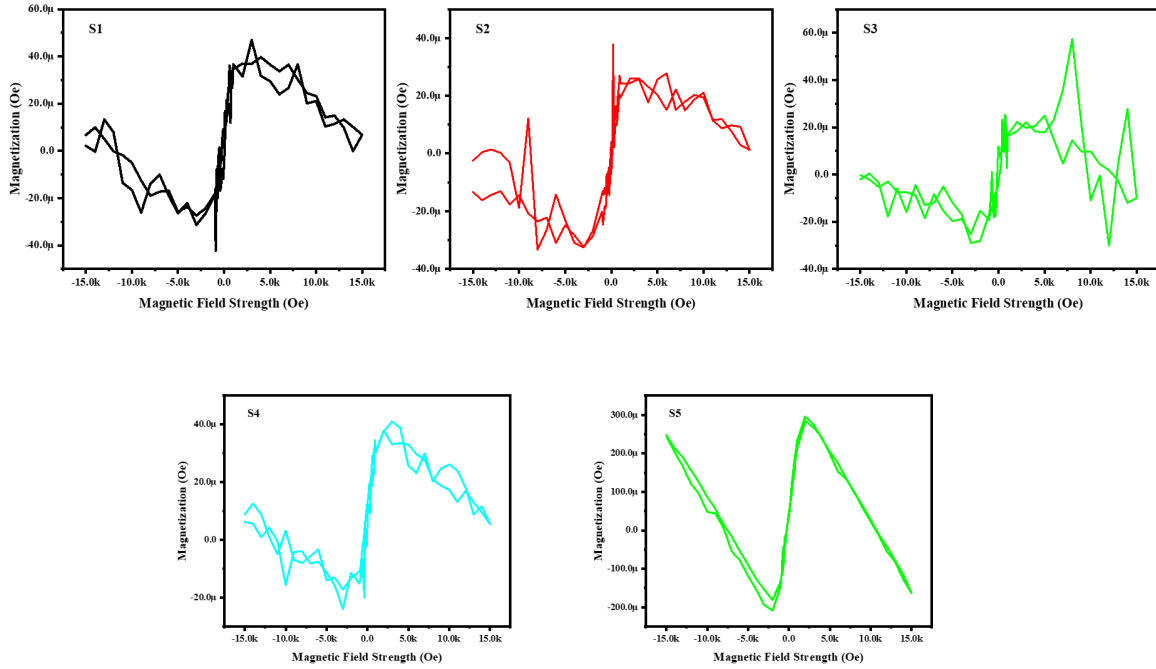


Fig 6.6: Plot of M-H Hysteresis loop for all samples

No evidence of magnetism was observed in the sample, indicating the absence of magneto-electric coupling. Consequently, the sample is not suitable for applications as a multiferroic device. However doping smartly to both the site could give us some multiferroicity here.

Bibliography

- [1] Y.-H. Bing, A. A. Bokov, and Z.-G. Ye, “Diffuse and sharp ferroelectric phase transitions in relaxors,” *Curr. Appl. Phys.*, vol. 11, no. 3, pp. S14–S21, May 2011, doi: 10.1016/j.cap.2011.04.041.
- [2] M. Arshada, Wasi Khana et.al, “Correlation between structure, dielectric and multiferroic properties of lead free Ni modified BaTiO₃ solid solution” *Ceramics International* 46 (2020) 27336 - 27351.
- [3] C. Fu, N. Chen, and G. Du, “Comparative studies of Nickel doping effects at A and B sites of BaTiO₃ ceramics on their crystal structures and dielectric and ferroelectric properties,” *Ceram. Int.*, vol. 43, no. 17, pp. 15927–15931, Dec. 2017, doi: 10.1016/j.ceramint.2017.08.169.
- [4] C. Behera¹, P. Patel et.al, “ Studies of structural, dielectric and electrical characteristics of Nickel-modified Barium Titanate for device applications” , *J Mater Sci: Mater Electron* (2022) 33:1657–1669.
- [5] A. Jana a, T.K. Kundu, “ Microstructure and dielectric characteristics of Ni ion doped BaTiO₃ nanoparticles”, *Materials Letters* 61 (2007) 1544–1548.
- [6] Y. Qi, S. Liu, I. Grinberg, and A. M. Rappe, “Atomistic description for temperature-driven phase transitions in BaTiO₃,” *Phys. Rev. B*, vol. 94, no. 13, p. 134308, Oct. 2016, doi: 10.1103/PhysRevB.94.134308.
- [7]. https://en.wikipedia.org/wiki/Goldschmidt_tolerance_factor
- [8]Artemios Karvounis, Flavia Timpu, et.al, “Barium Titanate Nanostructures and Thin Films for Photonics” doi: <https://doi.org/10.1002/adom.202001249>
- [9]KATARZYNA TKACZ-SMIECH. A. KOLEZŃSKI and W.S. PTAK Chemical Bond in Ferroelectric Perovskites. *Ferroelectrics*, 2000. Vol 237. pp. 51-64.
- [10] ANDRZEJKOLEŃSKI AND KATARZYNATKACZ-SMIECH, “From the Molecular Picture to the Band Structure of Cubic and Tetragonal Barium Titanate”. DOI: 10.1080/00150190590926300
- [11] Katarzyna Tkacz-Smiech, Andrzej Koleźński*, W.S. Ptak, Crystal-chemical aspects of phase transitions in Barium Titanate, PERGAMON. *Solid State Communications* 127 (2003) 557–562.

- [12] P Maneesha et.al. Room temperature Multiferroicity and Magnetoelectric coupling in Ca/Mn modified BaTiO₃ arxiv.org 2410.22018v3
- [13] J. Akimoto, Y. Gotoh, and Y. Oosawa, “Refinement of hexagonal BaTiO₃.” Accessed: Oct. 14, 2024. [Online]. Available: <https://www.crystallography.net/cod/2009488.html>
- [14] Shannon radii : <http://abulafia.mt.ic.ac.uk/shannon/radius.php?Element=Ni>
- [15] B. Zalar, V. V. Laguta, and R. Blinc, “NMR Evidence for the Coexistence of Order-Disorder and Displacive Components in Barium Titanate,” *Phys. Rev. Lett.*, vol. 90, no. 3, p. 037601, Jan. 2003, doi: 10.1103/PhysRevLett.90.037601.
- [16] A. F. Devonshire, “Theory of ferroelectrics,” *Adv. Phys.*, vol. 3, no. 10, pp. 85–130, Apr. 1954, doi: 10.1080/00018735400101173.
- [17] W. Cochran, “Crystal stability and the theory of ferroelectricity” doi: <https://doi.org/10.1080/00018736000101229>
- [18] I. A. Santos and J. A. Eiras, “Phenomenological description of the diffuse phase transition in ferroelectrics,” *J. Phys. Condens. Matter*, vol. 13, no. 50, pp. 11733–11740, Dec. 2001, doi: 10.1088/0953-8984/13/50/333.
- [19] Urszula D. Wdowik¹, Krzysztof Parlinski, “ Soft-phonon mediated structural phase transition in GeTe” *Phys. Rev. B* 89, 224306
- [20] Puspa Upreti^{1,2}, Matthew Krogstad Order-Disorder Transitions in (Ca_xSr_{1-x})₃Rh₄Sn₁₃ *Phys. Rev. Lett.* 128, 095701
- [21] Ghosez, Philippe Proper, improper and hybrid improper ferroelectricity in oxide perovskites and related compounds American Physical Society arch 18-22, 2013, abstract id. A21.004
- [22] V. Dvořák, “Improper ferroelectrics” ,*Ferroelectrics* Volume 7, 1974 - Issue 1.
- [23] [https://phys.libretexts.org/Bookshelves/Thermodynamics_and_Statistical_Mechanics/Book%3A_Thermodynamics_and_Statistical_Mechanics_\(Arovas\)/07%3A_Mean_Field_Theory_of_Phase_Transitions/7.05%3A_Landau_Theory_of_Phase_Transitions](https://phys.libretexts.org/Bookshelves/Thermodynamics_and_Statistical_Mechanics/Book%3A_Thermodynamics_and_Statistical_Mechanics_(Arovas)/07%3A_Mean_Field_Theory_of_Phase_Transitions/7.05%3A_Landau_Theory_of_Phase_Transitions)
- [24] CHANG-RONG ZHOU* and XIN-YU LIU , “Dielectric properties and relaxation of Bi_{0.5}Na_{0.5}TiO₃–BaNb₂O₆ lead-free ceramics”, *Bull. Mater. Sci.*, Vol. 30, No. 6, December 2007, pp. 575–578.
- [25] Kenji Uchino a & Shoichiro Nomura ,”Critical exponents of the dielectric constants in diffused-phase-transition crystals”, *Ferroelectrics Letters*, 1982, Vol. 44, pp. 55-61.

- [26] Gerald Burns and F.H. Dacol, “ Crystalline ferroelectrics with glassy polarization behavior”, PHYSICAL REVIEW B VOLUME 28, NUMBER 5
- [27] ALEXEI A. BOKOV , and ZUO-GUANG YE, “DIELECTRIC RELAXATION IN RELAXOR FERROELECTRICS”, Journal of Advanced Dielectrics Vol. 2, No. 2 (2012) 1241010.
- [28] A. Fundora a b, A. Vázquez et.al, “Diffuse phase transitions in ferroelectric ceramics”, Journal of Non-Crystalline Solids, Volumes 235–237, 2 August 1998, Pages 567-569.
- [29] V A Isupov, “Some problems of diffuse ferroelectric phase transitions”, Ferroelectrics, Volume 90, 1989 - Issue 1.
- [30] Matthew Trainer, “Ferroelectrics and the Curie-Weiss law”, DOI: 10.1088/0143-0807/21/5/312
- [31] . G. A. Smolensky and V. A. Isupov, Soviet J. Techn. Phys., 24, 1375 (1954)
- [32] A. K. Tagantsev, “Vogel-Fulcher relationship for the dielectric permittivity of relaxor ferroelectrics“, Phys. Rev. Lett. 72, 1100.
- [33] Hewat, A.; David, W. I. F.; Eijck, L. van (1 August 2016). "Hugo Rietveld (1932–2016)". *Journal of Applied Crystallography*. **49** (4): 1394–1395. doi:10.1107/S1600576716012061. ISSN 1600-5767.
- [34] J. TAUC (a) et.al, “Optical Properties and Electronic Structure of Amorphous Germanium”, phys. stat. sol. 15, 627 (1966).
- [35] Vesna Džimbeg-Malčić et.al, “ KUBELKA-MUNK THEORYIN DESCRIBING OPTICAL PROPERTIES OF PAPER (I)”, ISSN 1330-3651 UDC/UDK 535.34/.36:676.017.55.
- [36] V. D. Mote, Y. Purushotham, and B. N. Dole, “Structural, morphological, physical and dielectric properties of Mn doped ZnO nanocrystals synthesized by sol–gel method,” Mater. Des., vol. 96, pp. 99–105, Apr. 2016, doi: 10.1016/j.matdes.2016.02.016.
- [37] Md. Parvez Ahmad, A. Venkateswara Rao, K. Suresh Babu, and G. Narsinga Rao, “Particle size effect on the dielectric properties of ZnO nanoparticles,” Mater. Chem. Phys., vol. 224, pp. 79–84, Feb. 2019, doi: 10.1016/j.matchemphys.2018.12.002.
- [38] Structure and Grain Size on Dielectric Properties of Manganese Ferrite (MnFe_2O_4) Nanoparticles,” IOP Conf. Ser. Mater. Sci. Eng., vol. 202, p. 012046, May 2017, doi: 10.1088/1757-899X/202/1/012046.

- [39] B. Sareni, L. Krähenbühl, A. Beroual, and C. Brosseau, “Effective dielectric constant of random composite materials,” *J. Appl. Phys.*, vol. 81, no. 5, pp. 2375–2383, Mar. 1997, doi: 10.1063/1.364276.
- [40] G. A. Mohamed, A. B. Abd El-Moiz, and M. Rashad, “Li-doping effects on the electrical properties of ZnO films prepared by the chemical-bath deposition method,” *Phys. B Condens. Matter*, vol. 370, no. 1–4, pp. 158–167, Dec. 2005, doi: 10.1016/j.physb.2005.09.006.
- [41] B. BISWAL and D. K. MISHRA, “Review on LCR measurement of dielectrics and analysis of various parameters “, *Orissa Journal of Physics* ISSN 0974-8202, Vol. 31, No. 1 February 2024 pp. 29 -42.
- [42] S. Ben Moumen, A. Neqali et al, “Impedance spectroscopy studies on lead free Ba_{1-x}Mgx(Ti_{0.9}Zr_{0.1})O₃ ceramics “, *Superlattices and Microstructures*.
- [43] Muzaffar Iqbal Khan and Trilok Chandra Upadhyay, “General Introduction to Ferroelectrics”, DOI: 10.5772/intechopen.97720
- [44] Xuanze Wang: Preparation, synthesis and application of Sol-gel method
- [45] Collected Papers of L. D. LANDAU, 1965.
- [46] Hirotaka et al, *Journal of the Physical Society of Japan* Vol. 56, No. 2, February, 1987, pp. 589-595.
- [47] FTIR Study of Nanostructure Perovskite BaTiO₃ Doped with Both Fe³⁺ and Ni²⁺ Ions Prepared by Sol-Gel Technique Vol. 126 (2014)
- [48] Choudhury et al. *International Nano Letters* 2013, 3:25
- [49] Kenji Uchino , Microscopic Region Effect on the Dielectric Property of the Diffused Phase Transition Ferroelectrics: A Reasonable and Effective Diffuseness Characterizing Parameter, DOI: 10.1111/j.1551-2916.2010.04224.x r2010 The American Ceramic Society
- [50] *J. Appl. Phys.* 136, 224101 (2024)
- [51] *Appl. Phys. Lett.* 91, 062908 (2007)
- [52] Vivek Dwij et al, *Physica B* 624 (2022) 413381

